Summer 9-12-2023

Patient-Specific Multi-Scale, Multi-Physics Simulations of Human Uterine Contractions and Peristalsis during Pregnancy and the Menstrual Cycle

Yiqi Lin
Washington University – McKelvey School of Engineering

Recommended Citation

Lin, Yiqi, "Patient-Specific Multi-Scale, Multi-Physics Simulations of Human Uterine Contractions and Peristalsis during Pregnancy and the Menstrual Cycle" (2023). *McKelvey School of Engineering Theses & Dissertations*. 958.
https://openscholarship.wustl.edu/eng_etds/958

WASHINGTON UNIVERSITY IN ST. LOUIS

McKelvey School of Engineering
Department of Electrical & Systems Engineering

Dissertation Examination Committee:
Yong Wang, Chair
Shantanu Chakrabartty
Neal Patwari
Chuan Wang
Qing Wang

Patient-Specific Multi-Scale, Multi-Physics Simulations of Human Uterine Contractions and Peristalsis during Pregnancy and the Menstrual Cycle

by
Yiqi Lin

A dissertation presented to
the McKelvey School of Engineering
of Washington University in
partial fulfillment of the
requirements for the degree
of Doctor of Philosophy

August 2023
St. Louis, Missouri

Table of Contents

List of Figures

List of Tables

Acknowledgments

First and foremost, I wish to extend my heartfelt gratitude to my advisor, Dr. Yong Wang. His unwavering support, guidance, and encouragement throughout these years have been invaluable. I consider myself fortunate to have been a part of his research group. His brilliance and innovative approach have consistently inspired me to push the boundaries of research. His optimism and consistent motivation have often been the beacon that guided me through challenges. I deeply appreciate all he has contributed to my academic journey.

My sincere thanks go to my committee members - Dr. Shantanu Chakrabartty, Dr. Neal Patwari, Dr. Chuan Wang, and Dr. Qing Wang. Their expertise, time, and invaluable feedback during my Ph.D. journey have significantly enriched my work.

I am indebted to my esteemed collaborators, Dr. Mariano Vázquez, Dr. Jazmín Aguado Sierra, Dr. Constantine Butakoff, and Dr. Beatriz Eguzkitza. Their continuous support and insightful suggestions have been pivotal to my research endeavors.

I express my appreciation to my labmates and friends whose assistance and support have greatly facilitated my research progress.

Special thanks are due to Dr. Deborah Frank and Mr. James Ballard for their efforts in polishing and refining my manuscripts.

Last but not least, my deepest gratitude goes to my family. To my parents, who always give me the strongest support in both good and challenging times. To my parents-in-law, for their unwavering support and encouragement. And most importantly, to my beloved wife, Lu Li, and our two children, who have been my source of love, motivation, and comfort. Your presence has illuminated every step of this journey.

This work was supported by WashU Startup Fund to Yong Wang.

Yiqi Lin

Washington University in St. Louis
August 2023

Dedicated to my family and my wife.

ABSTRACT OF THE DISSERTATION

Patient-Specific Multi-Scale, Multi-Physics Simulations of Human Uterine Contractions and Peristalsis during Pregnancy and the Menstrual Cycle

by

Yiqi Lin

Doctor of Philosophy in Electrical Engineering

Washington University in St. Louis, 2023

Professor Yong Wang, Chair

Uterine contractions during pregnancy drive birth, and peristalsis during menstrual cycles not only expel menstrual blood, but also play significant roles in both sperm transport and gynecological disorders. The present work encompasses an in-depth exploration into the electrophysiology, biomechanics, and fluid dynamics of these activities. We introduce an advanced multiscale dynamic electrophysiology model that delves into cellular-level details, using both electromyography (EMG) and cell force generation methods. An innovative ionic channel model integrates individual ionic channel knowledge and clinical data from the human myometrium. This model accurately represents action potentials and their interactions with oxytocin, while an associated mechanical force model illustrates the intricacies of cellular force and its transition to tissue levels. Simultaneously, to bridge a noted gap in research, the multi-scale, multi-physics "Alya Purple" computational framework was developed to simulate 3D human uterine peristalsis and contractions during both the menstrual cycles and pregnancy. This system relies on patient-specific data, merging clinical findings from both the electromyometrial imaging system (EMMI) and the uterine peristalsis imaging system (UPI). The flexibility of Alya Purple permits a multifaceted simulation, embracing electrical propagation, mechanical deformation, and fluid dynamics, and yielding invaluable insights into human uterine mechanisms. Collectively, these advances not only illustrate the

complex electrophysiological, biomechanical, and fluid dynamics of the uterus contractions and peristalsis but also hold promise for novel research directions, potentially offering strategies for managing gynecological disorders and preventing complications such as endometriosis and preterm births.

Chapter 1

Introduction

This dissertation commences with a chapter examining the anatomy and physiology of the uterus, then segues into an overview of uterine peristalsis and contraction mechanisms. An analysis of the electrophysiology of myometrial cells and tissues is bolstered by relevant experimental figures. The numerical methods utilized in the model developed in this project are also provided. Finally, the chapter examines the 3D imaging techniques used for the uterine study.

1.1 The uterus

The uterus, an organ in the female reproductive system, resembles a pear. Its upper segment, characterized by a rounded contour, constitutes both the fundus and the main body of the uterus. The extended lower segment of the uterus ends in the cervix [13]. Throughout pregnancy, the uterus substantially enlarges, increasing its weight by ten to twenty-fold within months. Following parturition, it typically returns to its pre-pregnancy state within a few weeks [41].

During each menstrual cycle, elevated levels of two key hormones, estrogen and progesterone, thicken the endometrium, the inner layer of the uterus, to foster potential fetal development. In the absence of fertilization, the endometrium, combined with blood and mucus from the vagina and cervix, is discharged via the vagina as menstrual flow [32][58]. During early pregnancy, the uterine wall significantly lengthens and thickens to accommodate the developing fetus. As gestation progresses and the fetus enlarges, the uterine wall continues to stretch. By the end of pregnancy, the uterine wall is only around 10 mm thick [64][14].

1.2 Uterine peristalsis during the menstrual cycle

During the reproductive years, the uterus of a non-pregnant woman undergoes frequent peristalsis driven by spontaneous mild contractions in the inner layer of the uterine smooth muscle. Ultrasound studies [48] [47] have revealed that, during the menses phase of the menstrual cycle, peristaltic waves predominantly travel from the fundus to the cervix. Conversely, during the ovulatory phase, peristalsis waves predominantly move from the cervix toward the fundus. These waves play a critical role in normal menstruation and fertility.

The direction of uterine peristalsis likely has functional consequences, and disruption of these patterns could contribute to pathologies [98] [6]. During the menses phase, fundus-to-cervix peristalsis waves likely help expel menstrual blood. During the ovulatory phase, cervix-to-fundus waves may help move sperm toward the fallopian tubes to promote fertilization [48] [47], and insufficient cervix-to-fundus peristalsis could contribute to infertility. Frequent or strong cervix-to-fundus peristaltic waves during the menses phase could cause retrograde menstruation and increase the risk of developing endometriosis [7][8][70]. In endometriosis patients, uterine peristaltic waves travel most frequently from the cervix toward the fundus during the menses phase [84].

1.3 Techniques for monitoring uterine peristalsis during menstrual cycle

There are several techniques for monitoring uterine peristalsis[47][75].

First, an intrauterine pressure catheter (IUPC) [75] can make high quality recordings of uterine peristalsis. However, IUPCs are invasive and may disrupt natural peristalsis patterns. Also, this invasive technique raises safety concerns, and many countries have discontinued its use.

A second possible monitoring technique, transvaginal ultrasound (TVUS) [85][66][46], is also invasive and lacks the sensitivity needed to pinpoint the site of peristalsis onset. Furthermore, the reliability of TVUS measurements is heavily influenced by the transducer's orientation, resulting in high subjectivity and time dependency [29].

A third technique, hysterosalpingography (HSSG) [45], uses X-rays to visualize a radiographic contrast dye injected into the uterus and fallopian tubes. Despite HSSG's objectivity, it cannot measure peristaltic amplitude or frequency. Additionally, radiation exposure poses a potential risk, which also limits the duration of imaging.

A fourth technique, cine magnetic resonance imaging (MRI) [44][60][52][73], detects uterine peristalsis by capturing sequential images over an extended period and subsequently playing back the MRI frames at 12 times their actual speed. Nevertheless, extended cine MRI is expensive, time-consuming, operator-dependent, and lacks the capacity to identify the initiation and termination sites of uterine peristalsis.

Lastly, our lab has developed uterine peristalsis imaging (UPI) [84] a safe, comfortable, and accurate technique. UPI provides precise quantitative electrophysiological evidence that uterine peristalsis changes in frequency, direction, duration, magnitude, and power throughout the menstrual cycle. In UPI, magnetic resonance imaging (MRI) first defines the body/uterus geometry. Then, electrodes placed on the body surface measure endogenous uterine electrical activity for 30 minutes during each of the four menstrual phases. Finally, UPI software combines the MRI and electrophysiological datasets to map the electrical activity onto the uterus in three dimensions. UPI studies performed on 17 reproductive-age participants with normal menstruation found that during the menses phase, uterine peristaltic waves traveled most frequently from the fundus toward the cervix, whereas during the ovulatory phase, the waves traveled most frequently from the cervix toward the fundus. A schematic of uterine peristalsis imaging is shown in Fig 1.1.

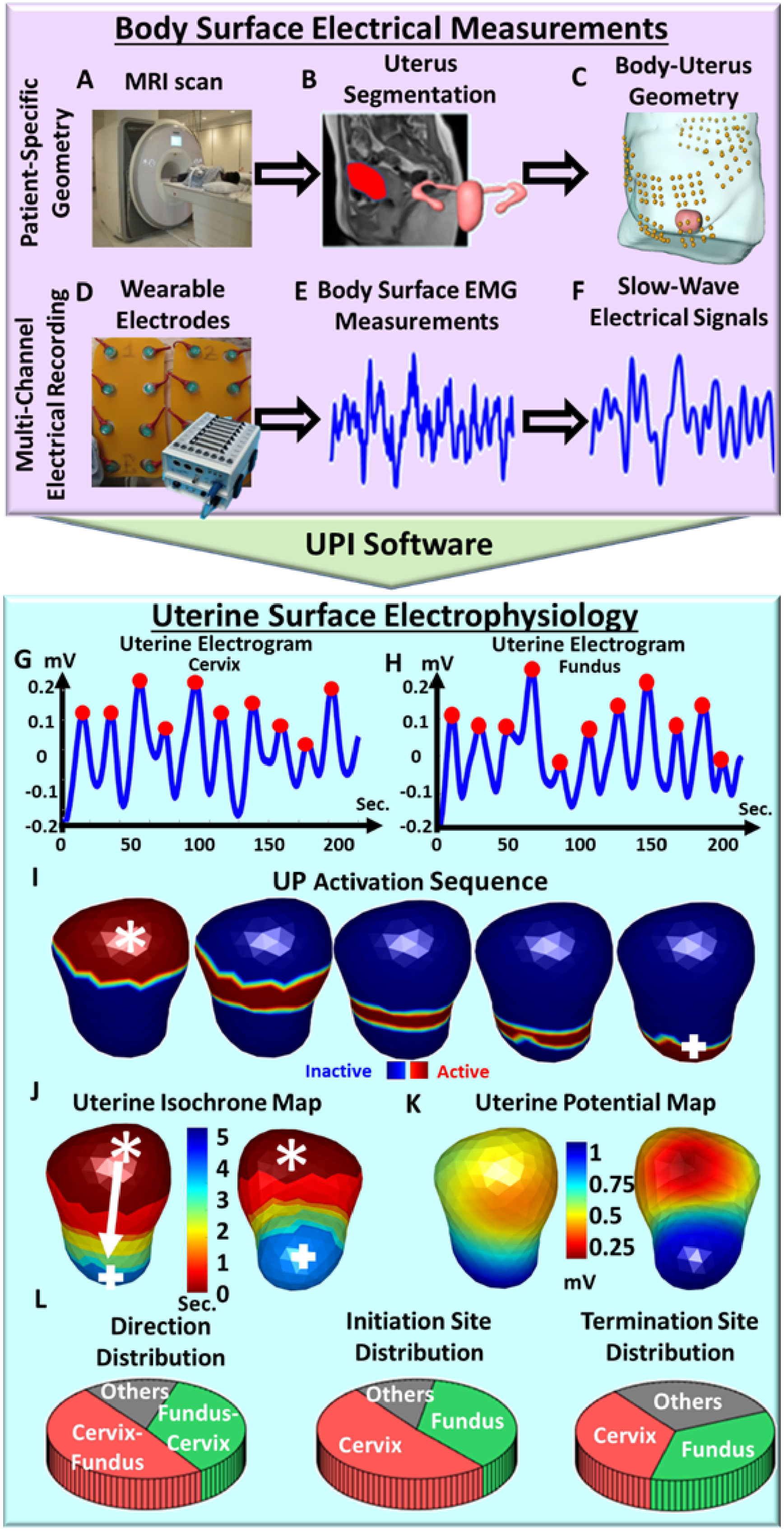
Body Surface Electrical Measurements
Patient-Specific Geometry
A MRI scan
B Uterus Segmentation
C Body-Uterus Geometry
Multi-Channel Electrical Recording
D Wearable Electrodes
E Body Surface EMG Measurements
F Slow-Wave Electrical Signals
UPI Software
Uterine Surface Electrophysiology
G mV
Uterine Electrogram
Cervix
0.2
0.1
0
-0.1
-0.2
Sec.
0
50
100
150
200
H mV
Uterine Electrogram
Fundus
0.2
0.1
0
-0.1
-0.2
Sec.
0
50
100
150
200
I
UP Activation Sequence
Inactive
Active
J
Uterine Isochrone Map
5
4
3
2
1
0
Sec.
K
Uterine Potential Map
1
0.75
0.5
0.25
mV
L
Direction Distribution
Others
Fundus-Cervix
Cervix-Fundus
Initiation Site Distribution
Others
Fundus
Cervix
Termination Site Distribution
Others
Cervix
Fundus

Figure 1.1: **Schematic of uterine peristalsis imaging.** (A) A brief anatomical MRI determines the uterus-body surface geometry. (B) Segmentation of the body surface, uterine surface, and fallopian tubes. (C) Patient-specific body-uterus geometry. (D) Electrode patches placed on the patient's abdomen and back record body surface electrical signals. (E) Electrical signal measurements on the patient's body surface. (F) Filtered electrical signals (bandwidth: 0.01-0.1 Hz). (G) Uterine surface electrical signals from one uterine surface point around the fundal region. Red dots denote the points of steepest negative slope to represent the activation times during peristalsis cycles. (H) Uterine surface electrical signals from one uterine surface point around the cervical region. (I) Detailed activation sequence of one complete uterine peristalsis cycle initiated near the fundus and terminated near the cervix. (J) Uterine isochrone maps from the same uterine peristalsis cycle. Warm and cool colors represent early and late activation, respectively. The white arrow depicts the peristalsis propagation direction. (K) One instant uterine potential map from the same uterine peristalsis cycle in I and J represents the potential distribution over the entire 3D uterine surface. (L) Distribution of uterine peristalsis directions (cervix-fundus, fundus-cervix, others), initiation and termination sites (cervix, fundus, and other areas) analyzed from one electrical mapping. Three other electrophysiological indices—the magnitude, duration, and power of the uterine peristalsis—were also generated

1.4 Uterine contractions during pregnancy

Uterine contractions during normal pregnancy and preterm birth serve a fundamental role in expelling the fetus from the uterus. Concurrently, they also help mitigate the risk of postpartum hemorrhage. In conventional labor, a rhythmic pattern of 3 to 5 contractions, each lasting for approximately 30 to 40 seconds, occurs in a ten-minute period [57].

Early indicators of preterm labor often include experiencing six or more uterine contractions within a single hour. Spontaneous preterm labor, defined by the onset of premature contractions and changes in cervical conditions without the premature rupture of the amniotic membrane, contributes to approximately half of all preterm births [2]. On occasion, preterm contractions might not result in immediate delivery, indicating underlying issues or disturbances that may not be sufficiently severe to precipitate immediate birth. However, these minor disturbances can potentially escalate over time, leading to unfavorable outcomes if not adequately managed [20].

Thus uterine contractions, whether at term or preterm, can profoundly affect maternal and fetal health, and must be carefully monitored and evaluated.

1.5 Techniques for monitoring uterine contractions during pregnancy

The tocodynamometer (TOCO) [30] [43] [62][34], which measures the pressure exerted by the contracting abdomen, has been widely used in the labor & delivery unit to evaluate uterine contractility. This non-invasive monitoring technique employs a pressure transducer positioned on the patient's abdomen, and it remains useful throughout all stages of labor. However, TOCO monitoring cannot provide quantitative measurements of contraction intensity, and it provides only a single global measure of uterine pressure. Furthermore, the device can be inaccurate and the tightness of the applied belt introduces variability.

Unlike the TOCO, the intrauterine pressure catheter (IUPC) [22][43][51], which is often regarded as the gold standard, quantitatively measures contraction intensity. However, using an IUPC assumes that amniotomy has been performed. Proper placement of an IUPC requires proficiency, so there is a learning curve associated with this technique. As many as 30% placements have been reported as "extra membranous," thereby heightening the risk of artefactual waveforms, placental perforation, abruption, and even uterine rupture. Although the IUPC offers greater reliability and provides valuable information about contraction pressure, its invasive nature creates clinical risks.

As a superior alternative to a TOCO or an IUPC, our lab developed electromyometrial imaging (EMMI) to non-invasively and precisely record three-dimensional (3D) uterine electrical activation during contractions in sheep [88][83][81]. Subsequently, we developed a human-compatible EMMI system [82] to visualize and assess 3D patterns of uterine electrical activation with high spatial and temporal precision during full-term human labor. The human EMMI system integrates patient-specific anatomical structures of the body and uterus, and it harnesses multi-channel electrical measurements from up to 192 electrodes on the body's surface. The objective is to comprehensively reconstruct electrical activities across the three-dimensional uterus in a sequence of frames. The pipeline of the human EMMI system is shown in Fig1.2.

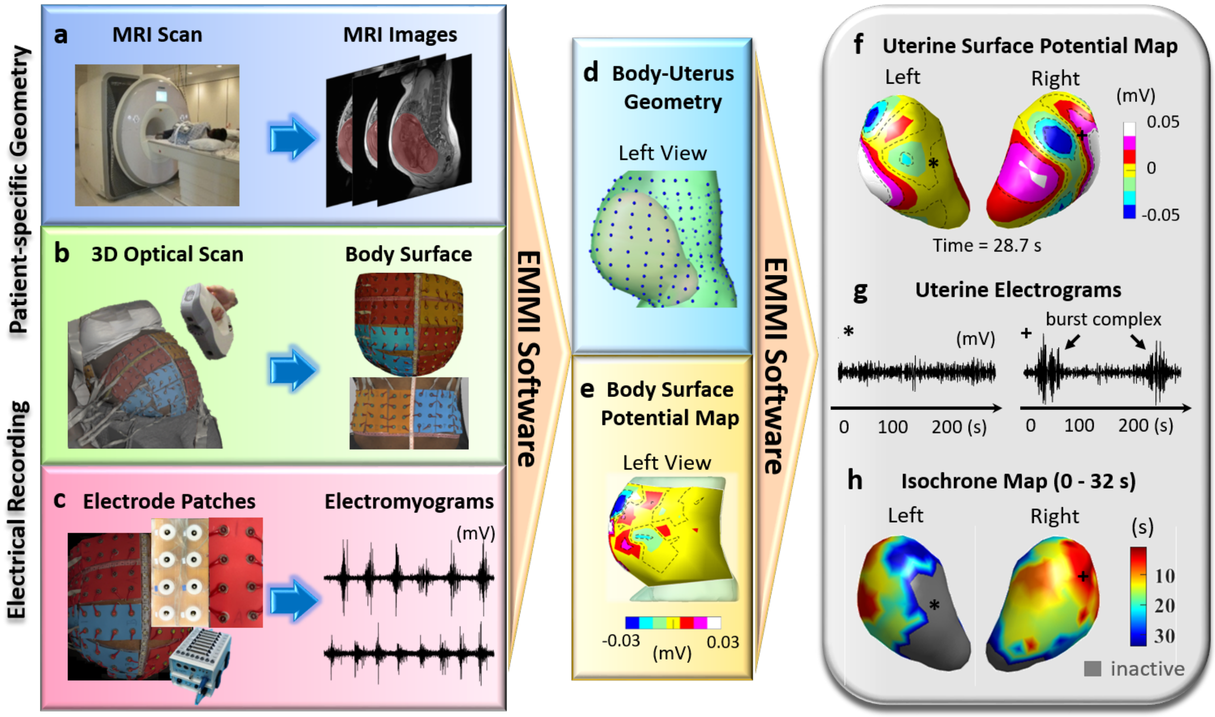

Figure 1.2: **Pipeline of the human EMMI system.** (a) An MRI scan is performed while the subject is wearing up to 24 MRI patches containing up to 192 markers. (b) An optical 3D scan of the body surface is performed while the subject is wearing electrode patches in positions corresponding to the positions of the MRI patches. (c) Body surface electromyograms are simultaneously recorded from up to 192 pin-type unipolar electrodes assembled as patches. EMMI generates (d), a body-uterus geometry from MR images with electrode locations on the body surface and, (e) a body surface potential map by rendering the electromyograms at each electrode at an instant in time on the body surface. EMMI combines the two datasets to reconstruct (f) uterine surface potential maps (electrical activity across the uterus at a single time point). With the potential maps, we can generate electrograms (g) of the electrical waveforms over time at each uterine site, and then derive (h), the uterine region, and the chronological sequence of electrical activation visualized as isochrone maps in 3D.

1.6 Organization of the dissertation

The rest of the dissertation is organized as follows. In Chapter 2, an ionic channel model is presented. In Chapter 3, Alya Purple simulations for uterine peristalsis during the menstrual cycle are conducted. In Chapter 4, Alya Purple simulations for uterine contraction during pregnancy are conducted. In Chapter 5, we summarize the contributions of this dissertation and discuss future directions.

Chapter 2

Electro-Mechanical Ionic Channel Modeling for Uterine Contractions and Oxytocin Effect during Pregnancy[1]

After a brief overview of ionic channel modeling, this chapter focuses on cellular level phenomena and the use of electromyography (EMG) and cell force generation methods to construct a new ionic channel model and a corresponding mechanical force model. The ionic channel model incorporates knowledge of individual ionic channels, including the electrochemical and bioelectrical characteristics of individual myocytes. Based on experimental data from the human myometrium, we develop a new sodium channel and a new potassium channel, with average human data correlations of 0.9946 and 0.9945, respectively. The model can generate single spike, plateau, and bursting action potentials. Moreover, it incorporates the effect of oxytocin in altering the properties of L-type and T-type calcium channels and further influencing the output action potentials. In addition, based on the new ionic channel model that describes detailed ionic dynamics, we develop a mechanical force model that describes the cellular mechanical force that propagates to the tissue level. We illustrate the relationship between the cellular mechanical force and the intracellular ionic dynamics and discuss the relationship between the application of oxytocin and the output mechanical force. Using sensitivity analysis, we also propose a simplified version of the model to enable large-scale simulations. Our results show that the model is able to usefully reproduce the bioelectrical and electromechanical characteristics of uterine contractions during pregnancy.

---

[1] This chapter is based on Lin, Yiqi, et al. "Electro-mechanical ionic channel modeling for uterine contractions and oxytocin effect during pregnancy." *Sensors* 19.22 (2019): 4898.

2.1 Overview of ionic channel modeling

Here, we briefly describe prior ionic channel models, then detail our approach in this work.

2.1.1 Previous approaches

An ionic channel model describes the natural biological behavior of cells in the uterus and their altered behavior after the clinical application of oxytocin. Previous studies have indicated that myocytes in the uterus can generate different types of action potentials [87, 42, 13]. Several mathematical models describe the electrostatics of ionic channels [53, 89, 90], basically illustrating the relationship between an input stimulus and the output membrane potential. However, most of these models are dimensionally limited and cannot fully express the biological properties of the ionic channels. Earlier mathematical models of action potential do include descriptions of many individual ionic channels [77, 76, 54], but the numerous individual channels made the whole model too complex, which limited its application as a forward model of 3D uterine contractions. As an additional limitation, there is little work focusing on the cellular-level influence of oxytocin on uterine contractions during pregnancy.

2.1.2 Our approach

In recent studies [49, 97, 96], we developed a multiscale model incorporating electrophysiological, anatomical, and magnetomyographic knowledge [21, 19]. This model amalgamated uterine contraction information at the cellular, tissue, and organ levels. However, the model did not accommodate specific ionic channels at the cellular level. To bridge this gap, we present an enhanced model incorporating several additional ionic channels whose behavior is described by potassium and sodium data obtained from the human myometrium.

These channels, founded on the Hodgkin and Huxley equations [33], are adjusted to align with laboratory data on individual ionic currents relative to a range of membrane potential values. We integrated these channels into the existing framework of Tong's model [77], replacing the original ones with our newly developed channels supported by recent human myometrial data. The revamped ionic channel model can generate single spike, plateau-type, short burst, and long burst action potentials, corroborating previous studies [42, 13].

Recognizing the constant evolution of the mechanical properties of the myometrium during gestation [92], we incorporated a mechanical force model derived from Hai and Murphy's studies [31] on smooth muscle cells. This model effectively produces cell mechanical force based on the newly developed ionic channel model, contributing to our understanding of cell force generation and its implications for uterine contractions.

In light of Mironnear's [59] and Nakao's studies [61] demonstrating the effects of oxytocin on calcium channel current and the action potential, we also introduce a new oxytocin model to simulate these experimental observations. Our model regards oxytocin as a clinical intervention tool, able to control calcium current and subsequently influence the calcium concentration, action potential generation, and force generation.

In summary, we propose a forward model that is capable of reproducing the characteristics of uterine contractions. We introduce an ionic channel model, an oxytocin model, and a mechanical force model. These models elucidate the mechanism of each individual ionic channel, as well as the mathematical expression of the whole system. Thus, the results of this work can help us better understand the mechanisms of uterine cells, their force generation process, and the results of applying oxytocin. Understanding these mechanisms is clinically important in avoiding and treating complications such as preterm birth and abnormal uterine contractions, which can lead to significant medical and financial consequences [56, 69, 17, 74].

2.2 Uterine ionic channel modeling and the oxytocin effect

In the following section, we introduce a series of innovative uterine ionic channels. These channels underpin the intricate ionic system within uterine myocytes. Each channel within this complex system is simulated independently to ensure an accurate alignment with distinguishing feature points derived from a comprehensive set of laboratory data, graciously shared by our collaborator, Dr. Sarah England.

The data acquisition was conducted in full accordance with the Declaration of Helsinki, and the research protocol was approved by the Institutional Review Board at the Washington University School of Medicine (approval no. 201108143), except for registration in a database.

Our analysis incorporates representative recordings from four individual patients, each of whom provided written informed consent, thereby affirming their voluntary participation in our study. The consent form complied with guidelines provided by the Washington University in St. Louis Internal Review Board. Further details of the experimental setup, procedures, and subsequent data analysis are in [23].

Our ionic channel model primarily focuses on the sodium channel, potassium channel, and calcium channel, which together determine depolarization and repolarization during the generation of the action potentials in uterine contractions. This multi-faceted model was partly inspired by the Tong's model [77], but for several of the channels in Tong's original model we substituted our newly developed counterparts, enhancing its performance and accuracy.

Additionally, our model incorporates the influence of oxytocin, a key hormone in childbirth, on the ionic channels. This incorporation allows for a more dynamic and realistic representation of uterine contractions. We further expanded the scope of our study by introducing a mechanical force model to efficiently and accurately characterize the force dynamics during uterine contractions.

2.2.1 The sodium channel

The sodium channel is largely inactivated at resting potential. When it is activated, a significant number of sodium ions move into the cell, creating the rising phase of the action potential during depolarization. In our model, the sodium channel is built from raw lab data, recorded by our collaborator [23], from sodium channels in the uterine cells of human myometrial tissue samples from the lower uterine segments. The membrane potential and the solutions were designed to minimize the contribution of the calcium and potassium channels. Here, voltage-clamp sodium experimental data illustrate the electrical properties of sodium currents with respect to the membrane voltage values.

The model is fitted by Hodgkin and Huxley's equations for the sodium channel [33]. The sodium channel is represented by the nonlinear conductance g_{Na}, which depends on both time and voltage. To make this clear, we represent it by using the variable x_{Na}. Here x_{Na} depends only on time and voltage [53]. Thus, the nonlinear sodium conductance is given by

$$g_{\mathrm{Na}} = x_{\mathrm{Na}}\bar{g}_{\mathrm{Na}}. \tag{2.1}$$

We use m as an activation parameter and h as an inactivation parameter to describe the variable x_{Na}. Here, the sodium channel current is given by

$$I_{\mathrm{Na}} = m^3 h \bar{g}_{\mathrm{Na}}(V - E_{\mathrm{Na}}), \tag{2.2}$$

$$\frac{dm}{dt} = \frac{m_\infty - m}{\tau_m}, \tag{2.3}$$

$$\frac{dh}{dt} = \frac{h_\infty - h}{\tau_h}, \tag{2.4}$$

where m_∞ and h_∞ are the steady state values of m and h, given a relatively long time; τ_m and τ_h are time constants which describe how fast m and h will approach the steady state; V is the applied voltage; and E_{Na} is the resting potential, which is a constant value given by the Goldman equation [28]. Here m_∞, h_∞ and the time constants are functions of the applied voltage V and follow the Boltzmann's principle [26].

Accordingly, the ratio of the probabilities of a cell being in the membrane (P_1) and out of the membrane (P_2) follows an exponential function:

$$\frac{P_1}{P_2} = \exp(f(V)). \tag{2.5}$$

For one particular cell, the sum of the probabilities should be one, that is, $P_1 + P_2 = 1$, which gives us

$$P_1 = \frac{1}{1 + \exp(f(V))}. \tag{2.6}$$

Thus, for the steady state, the values of the active parameter and inactive parameter can be described in the following form:

$$m_\infty = 1/\left[1 + \exp(f_1(V))\right], \tag{2.7}$$

$$h_\infty = 1/\left[1 + \exp(f_2(V))\right], \tag{2.8}$$

where $f_1(V)$ and $f_2(V)$ are functions that depend on the membrane potential. The functions can be expressed by the difference between the current membrane potential and the membrane potential at which 1/2 activation occurs [94]. We obtained the mathematical formulations of these equations from our lab data.

2.2.2 The potassium channel

Potassium channels are classified by their biological properties. The most significant contributions come from the calcium-activated potassium channel, voltage-gated potassium channel, inward rectifier potassium channel, A-type transient potassium channel, and the background potassium leakage channel.

In our model, the potassium channel is built from raw lab data recorded by our collaborator under the experimental conditions described in [23]. The data came from potassium channels in the uterine cells of human myometrial tissue samples from the lower uterine segment. The patients were non-laboring women at term who had had Caesarean sections under spinal anesthesia. The recording focused on the potassium channel, so the membrane potential and the solutions were designed to minimize the contributions of the calcium and sodium channels.

Like the sodium channel, the potassium channel is represented by the nonlinear conductance g_{K}, which we represent by a variable x_{K}, which depends on time and voltage [53]. Thus, the nonlinear potassium conductance is given by

$$g_{\mathrm{K}} = x_{\mathrm{K}}\bar{g}_{\mathrm{K}}, \tag{2.9}$$

where x_K is illustrated by the activation parameter n and inactivation parameter q. Hodgkin and Huxley proposed that four activation gates control the potassium channel [33]. From the lab data, we found that the activation process is relatively faster than inactivation, so we used one inactivation gate to control the potassium channel. Therefore, the total current of the potassium channel is given by

$$I_{\mathrm{K}} = x_{\mathrm{K}}\bar{g}_{\mathrm{K}}(V - E_{\mathrm{K}}) = n^4 q\bar{g}_{\mathrm{K}}(V - E_{\mathrm{K}}), \tag{2.10}$$

where E_{K} is the resting potential given by the Goldman equation. We describe the activation and inactivation gate variables by the following first order differential equations:

$$\frac{dn}{dt} = \frac{(n_\infty - n)}{\tau_n}, \tag{2.11}$$

$$\frac{dq}{dt} = \frac{(q_\infty - n)}{\tau_q}, \tag{2.12}$$

where n_∞ and q_∞ are the steady state values and τ_n and τ_q are time constants which describe how fast n and q will approach the steady state. According to Boltzmann's principle, we describe the steady state values in the following equations:

$$n_\infty = 1/\left[1 + \exp(f_3(V))\right], \tag{2.13}$$

$$q_\infty = 1/\left[1 + \exp(f_4(V))\right], \tag{2.14}$$

where $f_3(V)$ and $f_4(V)$ are functions that depend on the membrane potential.

2.2.3 The calcium channel

Voltage-gated calcium channels are a group of voltage-sensitive ion channels located in the membranes of excitable cells. These channels open or close in response to changes in the electrical potential across the cell membrane, allowing the flow of calcium ions into or out of the cell. They activate upon membrane depolarization and mediate calcium influx in response to action potentials and subthreshold depolarizing signals [12].

The two major calcium channels are the L-type and T-type. L-type calcium channels are termed ”long-lasting” due to their slow inactivation kinetics and prolonged open-state during depolarization. These channels contribute significantly to the plateau phase of the action potential in smooth muscle cells. The influx of calcium ions via L-type channels also triggers calcium-induced calcium release from intracellular stores, amplifying the calcium signal and leading to muscle contraction. T-type calcium channels, the ”transient” type channels, are known for their fast activation and inactivation kinetics: they allow a quick and brief influx of calcium ions during the early phase of depolarization. These channels are implicated in pacemaking activities in the heart and neurons, contributing to the generation of regular electrical rhythms[55][12].

Here, we adopt Tong’s model [77] with regard to the L-type calcium channel and T-type calcium channel. The calcium currents are given by

$$I_{\mathrm{CaL}} = g_{\mathrm{CaL}} d^2 f_{\mathrm{Ca}} (0.8 f_1 + 0.2 f_2)(V - E_{\mathrm{CaL}}), \tag{2.15}$$

$$I_{\mathrm{CaT}} = g_{\mathrm{CaT}} b^2 g (V - E_{\mathrm{CaT}}), \tag{2.16}$$

where g_{CaL} and g_{CaT} are the calcium conductances; d and b are the activation gate variables; f_1, f_2 and g are the inactivation gate variables; f_{Ca} is the calcium inhibition; and E_{CaL} and E_{CaT} are the reversal potentials.

2.2.4 Oxytocin effect model

Pharmacologic stimulation of uterine contractions and the use of agents to promote cervical ripening are common procedures in obstetric practice. Oxytocin is commonly used for these purposes [3], and research on the oxytocin effect is clinically important. Our oxytocin model mimics the application of oxytocin as a clinical manual intervention, considering its influences on calcium concentration, membrane potential, and the mechanical force model. In previous studies, Mironnear [59] and Nakao [61] found that a low concentration of oxytocin caused a slight depolarization of the resting potential and consequent increase in the amplitude of the action potential (5 mV to 10 mV). A recent study by Ferreira et al. [23]showed that the activation of the oxytocin receptor inhibits SLO2.1 channels. This inhibition is linked to the opening of voltage-dependent calcium channels and the consequent increase of the intracellular calcium concentration (e.g., L-type and T-type). Buford's work [5] introduced the influence of oxytocin as a multiplier factor, using the sigmoid response on the conductivity of the L-type calcium channel.

Based on these experimental results, our oxytocin model was developed to increase both the L-type and T-type inward calcium currents by using an amplifier variable that controls the conductivity of these calcium channels. The amplifier is given by the following equation:

$$\mathrm{AM} = \frac{0.37}{1 + \exp - (\mathrm{oxy} - 0.946)} + 1, \tag{2.17}$$

$$\tilde{g}_{\mathrm{CaL}} = \mathrm{AM} \times g_{\mathrm{CaL}}, \tag{2.18}$$

$$\tilde{g}_{\mathrm{CaT}} = \mathrm{AM} \times g_{\mathrm{CaT}}, \tag{2.19}$$

where oxy represents the concentration of oxytocin applied in the experiment. The new L-type calcium conductance, $\tilde{g}_{\mathrm{CaL}}$ and T-type calcium conductance, $\tilde{g}_{\mathrm{CaT}}$, were calculated by the product of the amplifier, AM and the original calcium conductances, g_{CaL} and g_{CaT}. Note that, as we will show in our simplified model in Section 2.3.5, both L-type and T-type calcium channels are key elements in controlling the action potential.

In Equation (2.17), the amplifier is described using a sigmoid function [27], which can express the biological and electrical properties of the oxytocin application and also fits the experimental results. To fit the parameters, we used lab data from Nakao [61]. Also, applying oxytocin to the calcium channels increases the uterine mechanical force.

2.2.5 Uterine cell force model

Our uterine contraction force model is fundamentally designed around the concentration of calcium ions. This model is constructed on the premise that calcium-dependent myosin phosphorylation is the key driver behind the cyclical formation and breakage of cross-bridges in uterine smooth muscle tissue. This regulatory mechanism is crucial as it translates changes at the molecular level into macroscopic motion, essentially driving the contraction of the muscle.

In more detail [65], myosin phosphorylation is a biological process whereby a phosphate group is transferred to the protein myosin, a motor protein that is instrumental in muscle contraction. The rate and extent of this phosphorylation are tightly regulated by the concentration of calcium ions within the muscle cell. As the calcium concentration increases, typically in response to electrical signals, more myosin proteins undergo phosphorylation, which in turn induces the conformational changes necessary for the muscle to contract. As the calcium concentration decreases, the myosin proteins return to their resting state, allowing the muscle to relax. This calcium-dependent regulation of myosin phosphorylation gives muscle tissue, including the uterine smooth muscle, its ability to contract and relax in a controlled manner.

In our model, we adopted the cross-bridge model proposed by Hai and Murphy [31], which describes the kinetics of myosin phosphorylation. This model offers a detailed representation of how variations in calcium concentration drive the transition of myosin between its phosphorylated and dephosphorylated states, which in turn controls the formation and breakage of cross-bridges. By applying this model to the uterine smooth muscle, we can accurately describe how changes in calcium concentration during the female reproductive cycle induce rhythmic contractions of the uterus. Ultimately, this model provides a comprehensive understanding of how biochemical events at the cellular level result in the macroscopic phenomenon of uterine contractions.

Here, the model can be described by four differential equations:

$$\frac{d[\mathrm{M}]}{dt} = -K_1[\mathrm{M}] + K_2[\mathrm{Mp}] + K_7[\mathrm{AM}], \tag{2.20}$$

$$\frac{d[\mathrm{Mp}]}{dt} = K_4[\mathrm{AMp}] + K_1[\mathrm{M}] - (K_2 + K_3)[\mathrm{Mp}], \tag{2.21}$$

$$\frac{d[\mathrm{AMp}]}{dt} = K_3[\mathrm{Mp}] + K_6[\mathrm{AM}] - (K_4 + K_5)[\mathrm{AMp}], \tag{2.22}$$

$$\frac{d[\mathrm{AM}]}{dt} = K_5[\mathrm{AMp}] - (K_7 + K_6)[\mathrm{AM}], \tag{2.23}$$

where M is the detached dephosphorylated cross bridge, MP is the detached phosphorylated cross bridge, AMp is the attached phosphorylated cross bridge, AM is the attached dephosphorylated cross bridge, and K_1-K_7 are the rate constants.

2.3 Numerical examples and discussion

2.3.1 The sodium channel

From voltage clamp raw lab data, the activation and inactivation gate variables are fitted by the following equations:

$$f_1(V) = -\frac{V + 20.3}{6.2}, \tag{2.24}$$

$$f_2(V) = \frac{V + 46.2}{7.2}, \tag{2.25}$$

$$m_\infty = 1/\left[1 + \exp\left(-\frac{V + 20.3}{6.2}\right)\right], \tag{2.26}$$

$$h_\infty = 1/\left[1 + \exp\left(\frac{V + 46.2}{7.2}\right)\right]. \tag{2.27}$$

The efficacy of our model's depiction of sodium currents is explored by comparing the outcomes of the fitted model with the corresponding raw data. This comparison, as depicted in Figure 2.1a–c, extends across voltage clamp values from −40 mV to 0 mV, in steps of 20 mV. To enhance the comparability of the results, we normalize the current values featured on the vertical axis.

As Figure 2.1a–c demonstrate, the sodium currents modeled through our fitting procedure effectively mirror the raw data following the stimulus. The stimulus is applied at 11 ms, with the subsequent lab data revealing that the sodium current rapidly ascends to its peak value. This peak is then followed by a swift initial decay phase before the current eventually trails off towards a stable state at a more gradual rate. In our model, we have sought to accurately reflect these findings by assigning a low level to the time constant for the activation gate, denoted as τ_m, in contrast to the considerably higher level designated for the time constant of the inactivation gate, τ_h.

Within the studied range of voltage clamp values, the processes of activation and inactivation intrinsic to the sodium channel model are accurately fitted to the lab data, indicating the robustness of our model. To further validate the model's reliability, we calculated the correlation coefficients and the corresponding mean square errors of our simulation results in relation to the raw data, with both assessed at the same time steps. The calculated correlation coefficients of 0.9972, 0.9953, and 0.9912, coupled with the corresponding mean square errors of 0.0022, 0.0028, and 0.0035 for voltage clamp values of -40mV, -20mV, and 0 mV, respectively, attest to the reliability and consistency of our simulation models in reflecting the pattern observed in the raw lab data.

Moreover, we also examined the steady state values of both the activation gate and the inactivation gate, with the results presented in Figure 2.1d.

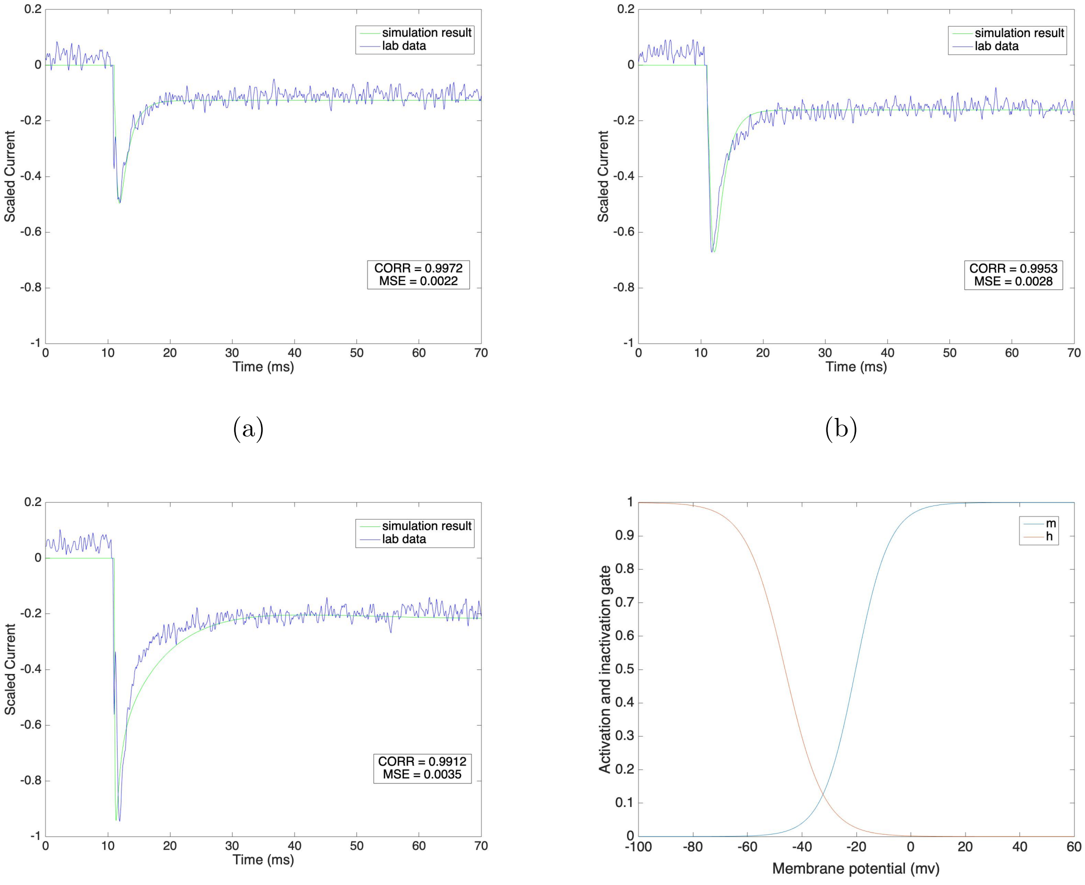

(a) (b)

(c) (d)

Figure 2.1: (**a**–**c**) Sodium current under different voltage clamp values(-40 mV, -20 mV and 0 mV). (**d**) Steady state of activation and inactivation gates dependent on membrane potential.

2.3.2 The potassium channel

In order to fit the potassium channel model with the lab data, we set certain conditions to closely depict the natural biological milieu. The recording data at our disposal captured the workings of the potassium channel within human myometrial smooth muscle cells (hMSMCs), and in order to avoid interference from other channels, we made certain that both calcium and sodium channels were inhibited during the experiment.

The experimental solution used was carefully formulated to maintain physiological relevance while still providing the isolation necessary for the experiment. The solution constituted symmetrical potassium, with a composition of 160 mM KCl, 80 mM NaCl, 10 mM Hepes, and 10 mM MES.

Furthermore, the pH of the solution was strictly maintained at 7.2, a physiological pH value closely matching that of the human body. This environment supported the correct functioning of cellular processes and interactions during the experiment. It not only helped generate reliable data but also enabled the fitted model to faithfully represent the biological dynamics of the potassium channel in the context of human myometrial smooth muscle cells.

Here, given the bio-electrical properties, the activation and inactivation gate variables are calculated by Boltzmann's principle [26]:

$$f_3(V) = -\frac{V+13}{13}, \tag{2.28}$$

$$f_4(V) = \frac{V+38}{6}, \tag{2.29}$$

$$n_\infty = 1/\left[1+\exp\left(-\frac{V+13}{13}\right)\right], \tag{2.30}$$

$$q_\infty = 1/\left[1+\exp\left(\frac{V+38}{6}\right)\right]. \tag{2.31}$$

The potassium channel model is informed by both lab data and simulations, which together paint a comprehensive picture of its behavior under different voltage clamp values. Figure 2.2a shows lab-recorded voltage clamp potassium currents that range from −20 mV to 60 mV, in steps of 20 mV. This lab data provides the real physiological responses of potassium channels to various voltage inputs, forming the empirical basis of our model.

Building on this, Figure 2.2b presents the simulation results for the potassium current under the same range of voltage clamp values as the lab data. These simulations, based on the constructed model, give us an opportunity to assess the accuracy of our model by comparing its predicted behavior with the observed lab data. In this regard, we evaluate the correlation and the corresponding mean square errors between the two data sets at equivalent time steps.

In our analysis, the average correlation across all voltage clamp values from -20 mV to 60 mV is 0.9945, demonstrating a strong correlation between the model's simulation results and the actual lab data. Further, the average mean square error is 0.0039, which indicates a high level of accuracy in the model's predictions.

In these results, we notice an interesting feature of the potassium channels: their inactivation process is relatively slower than their activation process. This observation aligns with our initial assumptions, further reinforcing the soundness of our model. Finally, Figure 2.2c and d illustrate the behavior of the activation and inactivation gate variables respectively, further underlining their dependence on the membrane potential.

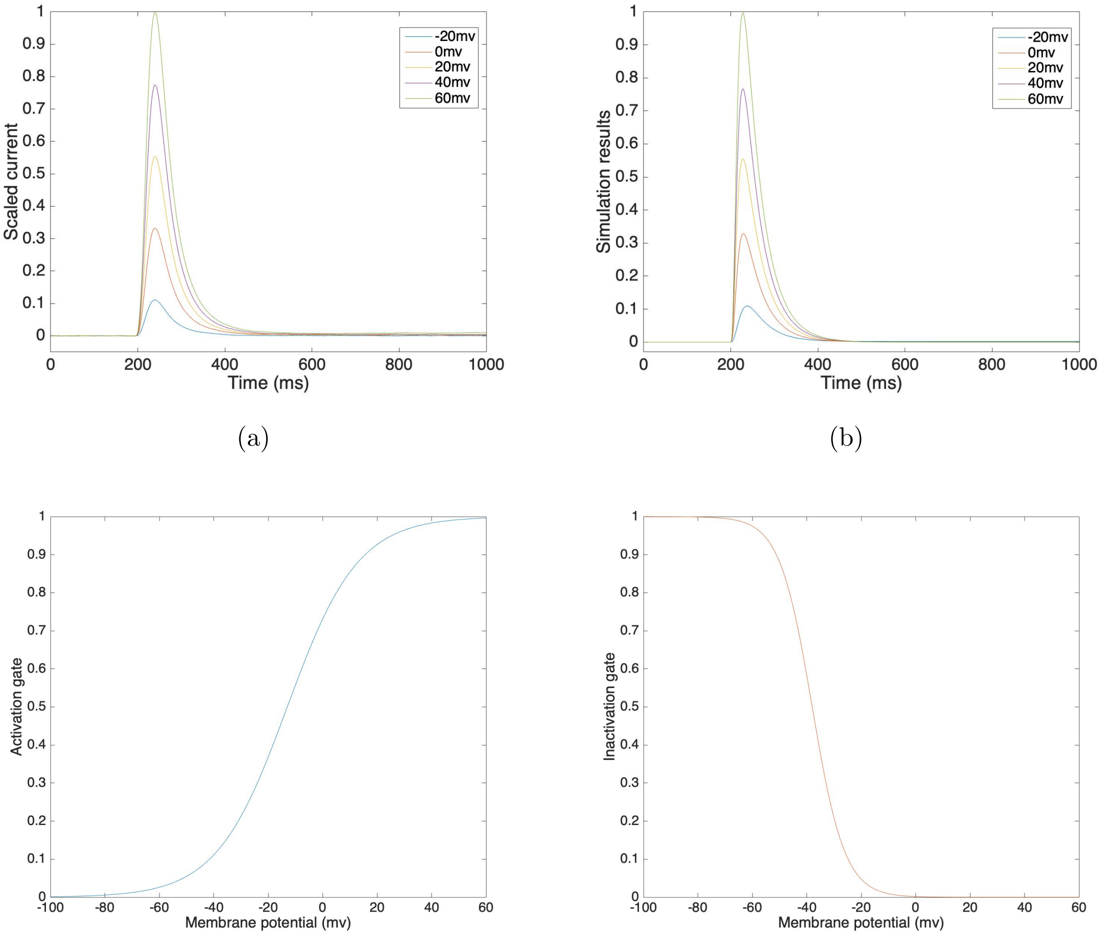

(a) (b)

(c) (d)

Figure 2.2: (**a**) Voltage clamp potassium channel lab data at voltage steps of −20 mV to 60 mV. (**b**) Voltage clamp potassium channel simulation result at voltage steps of −20 mV to 60 mV. (**c**) Simulated activation gate variable. (**d**) Simulated inactivation gate variable.

2.3.3 The oxytocin model

The oxytocin model we propose is designed to fit the amplitude changes observed in the action potential when different concentrations of oxytocin are applied. This model leverages the foundational structure of Tong's model [77], but with key modifications: we replace the sodium and K_1 potassium channels with the new channels that we've developed based on our lab data.

Figure 2.3a showcases the relationship between the value of the amplifier variable and the concentration of applied oxytocin. This graphical representation provides a quantifiable depiction of how the amplifier variable responds to varying levels of oxytocin, an integral aspect of the model.

Figures 2.3b and c present comparisons of the change in calcium concentration before and after the application of 1 µU/mL oxytocin. The two figures represent different types of action potentials: the plateau type action potential and the long burst type action potential, respectively. Interestingly, both these figures demonstrate that the application of 1 µU/mL oxytocin results in an increase in the peak of the calcium current by 20–40%. This simulated outcome aligns well with similar observations noted by Mironneau [59] under sodium-free conditions, which lends further validity to our model.

Figures 2.3d–f specifically illustrate the impact of oxytocin on a single spike of the action potential. Figure 2.3d depicts the original action potential without any oxytocin applied, serving as a control for the subsequent figures. Figure 2.3e and f represent the action potential under the influence of 1 µU/mL and 10 µU/mL oxytocin, respectively. By comparing these figures, we can discern the changes in the action potential induced by different concentrations of oxytocin, providing deeper insights into the functional role of this hormone.

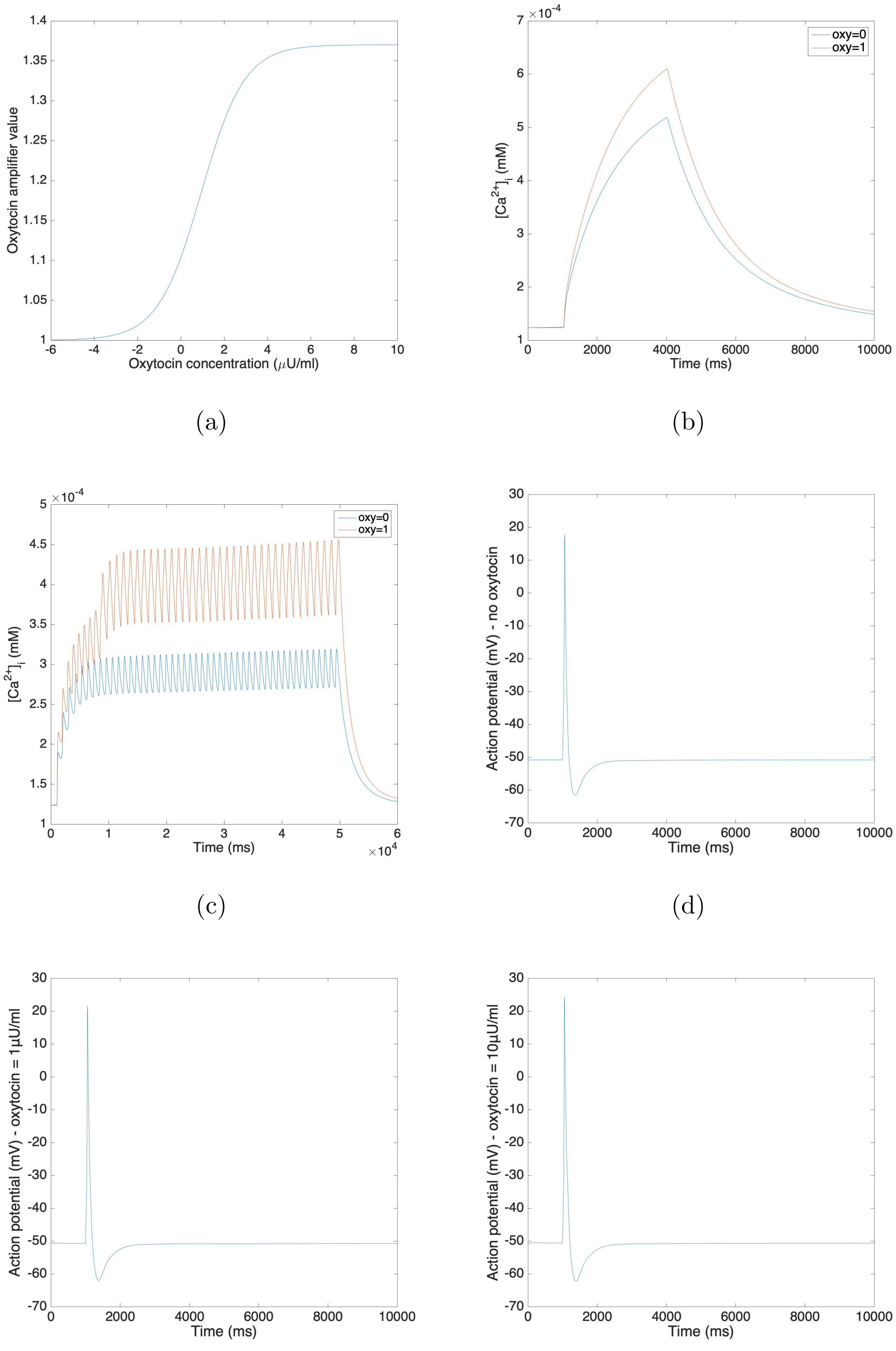

(a)

(b)

(c)

(d)

(e)

(f)

Figure 2.3: (**a**) Oxytocin amplifier value with respect to the concentration of oxytocin. (**b**) Change of calcium concentration of plateau type action potential under the application of 1µU/mL oxytocin. (**c**) Change of calcium concentration of long burst type action potential under the application of 1µU/mL oxytocin. (**d–f**) Action potentials under the application of different concentrations of oxytocin (no oxytocin, 1 µU/mL oxytocin and 10µU/mL oxytocin).

As illustrated in Figures 2.3b–f, the application of oxytocin indeed leads to an increase in both the calcium concentration and the amplitude of the action potential, while leaving the resting membrane potential virtually unchanged. Specifically, the application of 1 µU/mL oxytocin results in an increase in the amplitude of the action potential by 3.79 mV. Likewise, the application of 10 µU/mL oxytocin leads to an increase in the amplitude of the action potential by 6.65 mV. These simulation outcomes align well with the experimental data found in literature [61], further validating our model's effectiveness.

We also probe further into the changes in the action potential brought about by the application of differing amounts of oxytocin in Figure 2.4a,b. The simulation results illustrated in Figure 2.4a reveal that the amplitude of the action potential increases by 5–10 mV following the application of 0.2 µU/mL and 2 µU/mL oxytocin. Additionally, we note that the duration of the action potential lengthens as the concentration of applied oxytocin increases, a finding that corroborates with the experimental data from Mironneau [59] and Nakao [61].

Figure 2.4b further reveals the impact of applied oxytocin on long bursting action potentials. The simulation demonstrates an increase in the amplitude of each spike and a corresponding decrease in the time duration between each spike as oxytocin is applied. Again, these simulation results are consistent with Nakao's experimental results [61], further establishing the efficacy and reliability of our model.

2.3.4 Uterine cell force model

The mechanical force of uterine cells can be effectively represented by uterine cell stress, which is adjusted by a correlation coefficient. Building upon the experimental work of Hai and Murphy [31], we represent the smooth muscle stress as the sum of the attached phosphorylated cross bridge and the attached dephosphorylated cross bridge (AM+AMp). The development of force is then normalized using a correlation coefficient to align with experimental findings [9]. Moreover, our model illustrates how oxytocin application influences the development of force, providing additional insights into the complex dynamics of uterine contractions.

Figure 2.5 graphically demonstrates the development of force in both single spike and multiple spike action potentials. The solid line represents our model in the absence of oxytocin, while the dashed line indicates the model's behavior with an application of 1 µU/mL oxytocin. These force development simulation results closely replicate experimental results from Burdyga [9].

Upon the provision of stimulus, both the calcium concentration and the force display a rapid rise. Interestingly, the force takes more than 10 seconds to return to a steady state following this initial surge. Additionally, oxytocin application leads to an increase in the maximum calcium concentration by 10–20%, which in turn amplifies the force by 25–50%. These phenomena align well with existing experimental results from several research studies [4, 95].

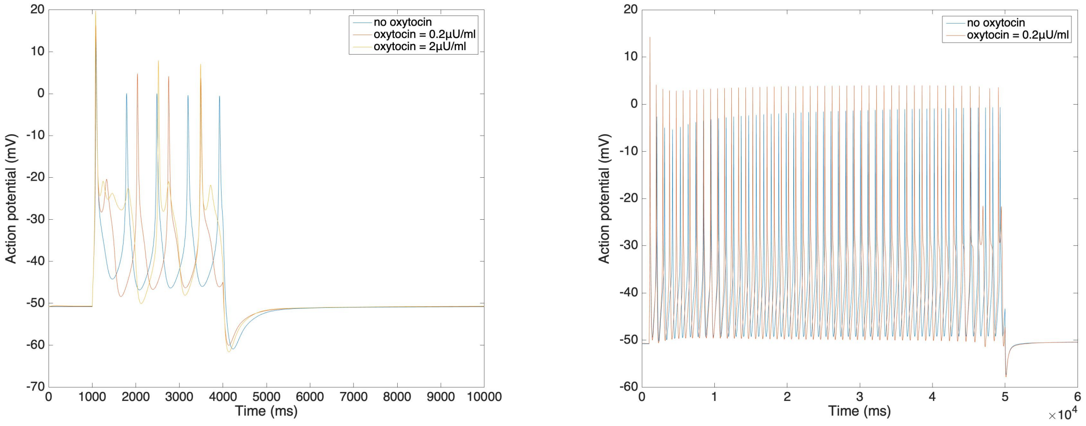

(a)

(b)

Figure 2.4: (**a**) Short burst action potential under the application of oxytocin at different concentrations. (**b**) Long burst action potential under the application of oxytocin.

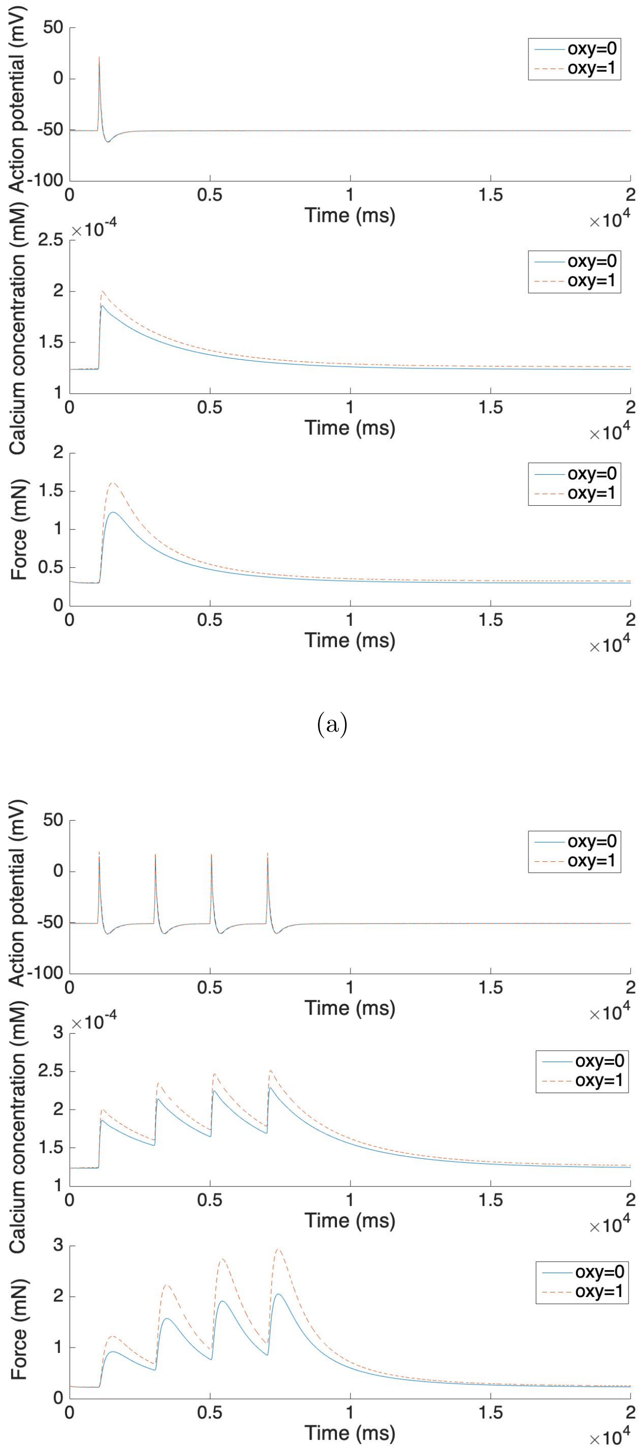

(a)

(b)

Figure 2.5: (**a**) Force development and oxytocin application of single spike action potential. (**b**) Force development and oxytocin application of four consecutive single spike action potentials.

2.3.5 Model simplification to enable large scale simulations

To conduct large-scale simulations, such as our previous work involving the 3D model [49, 97], the ionic channel model must be streamlined to reduce its dimensionality and the overall number of variables. We deploy Rihana's sensitivity analysis method [67] to prioritize the variables and subsequently perform a comprehensive stability analysis.

Our stability analysis initiates from an unstable steady state, a condition which often reveals interesting dynamical behavior. Next, we introduce a perturbation to each element of the main diagonal in the Jacobian matrix. What we record is the smallest absolute value of the perturbation that is capable of stabilizing the linearized system. This iterative method of sequentially perturbing and then observing changes allows us to systematically analyze the influence of individual parameters on the system's stability.

By this method, we are able to identify the most sensitive variables that significantly affect the system's behavior. These variables can then be prioritized in the simplified model. This approach offers a balance between computational feasibility and physiological accuracy, enabling us to run large scale simulations while maintaining the crucial aspects of the ionic channel model.

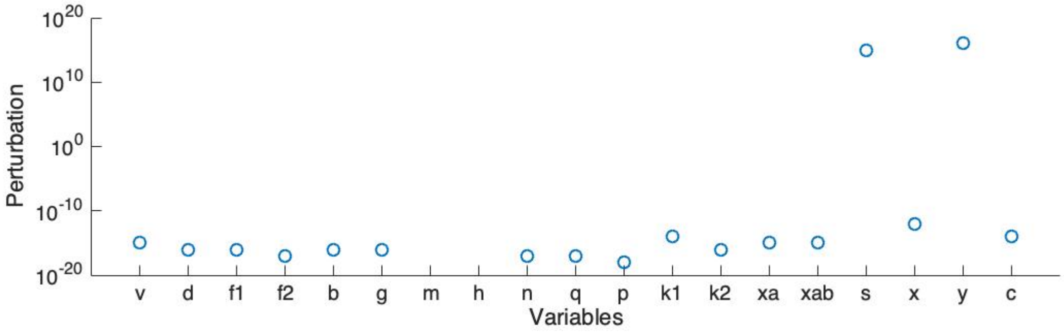

Figure 2.6: Stability analysis: smallest absolute values of perturbation on each variable which stabilize the system.

Figure 2.6 shows the smallest absolute values of perturbation on each variable which make all the eigenvalues of the Jacobian matrix have a negative real part. Here v represents the action potential; d, $f1$ and $f2$ represent the L-type calcium current; b and g represent the T-type calcium current; m and h represent the sodium current; y represents the hyperpolarisation-activated current; n and q represent the voltage-dependent potassium current K_1; p, $k1$ and

$k2$ represent the voltage-dependent potassium current K_2; s and x represent the transient potassium current; xa and xab represent the calcium-activation potassium current; and c represents the calcium-activated chloride current. Also, the back current, sodium potassium pump current and sodium calcium exchanger current are dependent on v; the non-selective cation current is dependent on both v and the calcium concentration.

The linearized model becomes stable if the perturbation is added on each element of the main diagonal of the Jacobian matrix. Based on this result, we select the variable pairs for which the corresponding perturbations are comparatively smaller than the others. We sort all the currents and choose the first four currents: the L-type calcium current (I_{CaL}), the T-type calcium current (I_{CaT}), the voltage-dependent potassium current K_1 (I_{K1}) and the voltage-dependent potassium current K_2 (I_{K1}). Also, we choose the non-selective cation current (I_{NSCC}), which has the largest magnitude. Therefore, there are 5 channels, represented by 13 variables, included in the simplified model. The simplified ionic channel model is described in the following equations:

$$I_{\text{sim}} = I_{\text{CaL}} + I_{\text{CaT}} + I_{\text{K1}} + I_{\text{K2}} + I_{\text{NSCC}}, \tag{2.32}$$

$$C_m \frac{dV_{\text{sim}}}{dt} = -I_{\text{sim}}, \tag{2.33}$$

$$V_{\text{ap}} = V_{\text{sim}} + V_{\text{b}}, \tag{2.34}$$

where I_{sim} is the total ionic current, which is a sum of the five chosen currents; C_m is membrane capacitance; V_{sim} is the membrane potential simulated by the five chosen currents; V_{b} is the background membrane potential, which is a constant value to offset the action potential; V_{ap} is the simulated output action potential. Note that I_{CaL} and I_{CaT} can be modulated by the oxytocin model in Equation (2.17). The following results do not include the application of oxytocin.

After the implementation of the simplified model, our analysis demonstrated that the model exhibits stability, which was determined using the Xppaut software [18]. This software tool allowed us to effectively calculate the new steady-state conditions for each of the variables within the model. The results of this analysis are presented in Figure 2.7, where action potentials under various conditions are graphically displayed.

Several action potentials were generated using MATLAB including single spike, plateau, and bursting types. These varied action potential simulations effectively recreate the unique electrical activities that are associated with uterine contractions, which are crucial in the understanding and analysis of this biological process.

To further validate our model, we compared its output with existing research. A study by Wilde et al.[87] provided values for the resting potential of this biological process, approximating it to around -45mV. Furthermore, this research stated that the plateau-type action potential typically spans a duration of about 5 seconds. Another source, a study by Casteels [11], informed us that the range of the action potential associated with uterine contraction is approximately 55 mV.

When comparing these previously reported figures to the outputs of our simplified model, we found a strong agreement. The resting potential calculated by our model was -44.9mV, which is nearly identical to the -45mV resting potential reported in the literature. Moreover, our model's action potential ranges were around 55 mV for all three cases, closely matching the value reported by Casteels. Finally, our model's time duration for the plateau-type action potential was exactly 5 seconds, which aligns perfectly with the reported duration from the Wilde et al. study.

The close alignment of these values with the literature gives us confidence in the accuracy of our simplified model, and suggests that it provides a reliable means of simulating the electrical activities of uterine contractions. This validation of our model is an important step towards more complex and large-scale simulations that can lead to a better understanding of the physiology of uterine contractions.

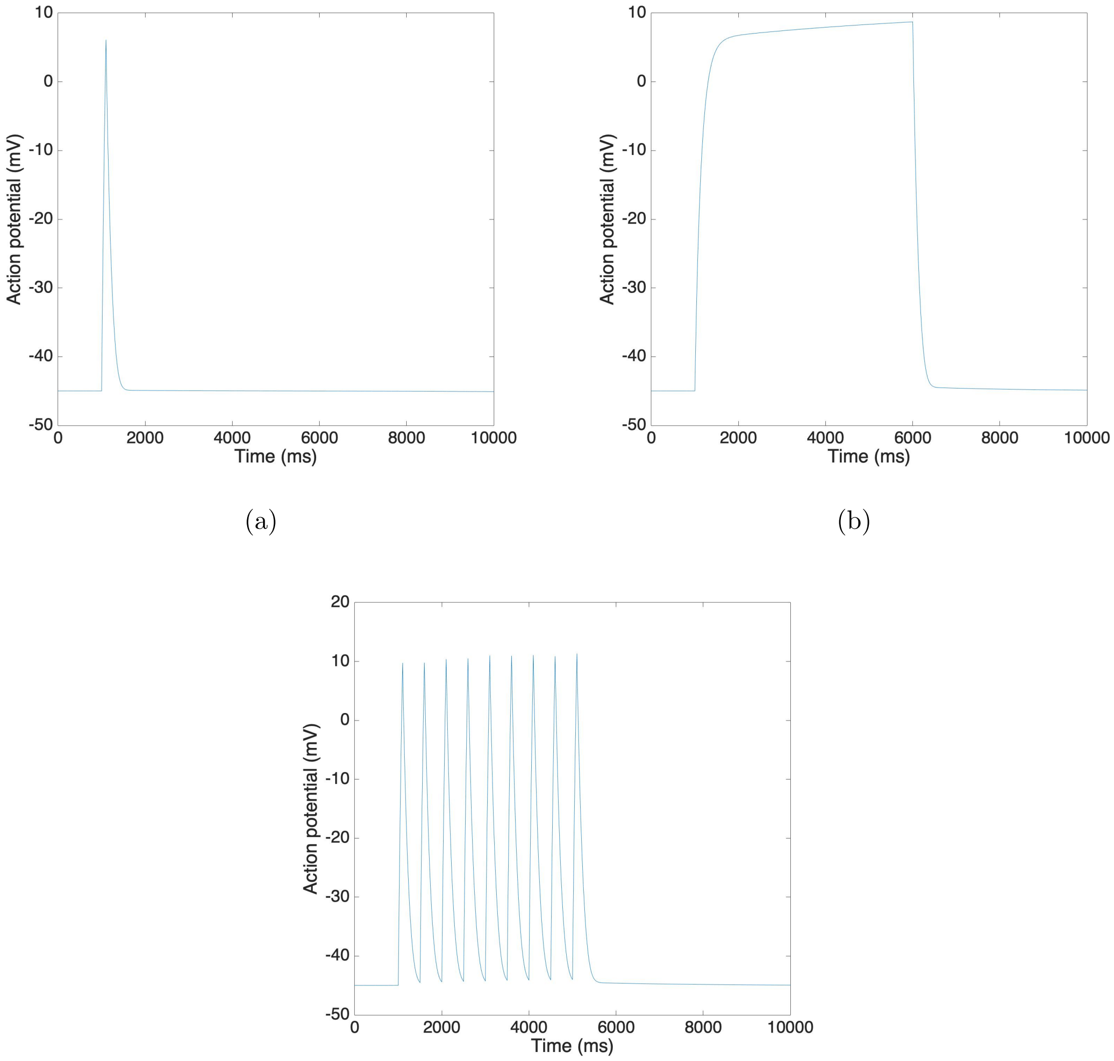

(a)

(b)

(c)

Figure 2.7: MATLAB simulation results of different types of action potential: (**a**) Single spike. (**b**) Plateau. (**c**) Bursting.

Following the simplification of the model, we implemented it into a 3D COMSOL spherical uterus model for simulation. Our 3D model incorporates both the newly developed ionic channel model and a multiscale forward electrical model. The detailed equations involved in the multiscale model are presented in Table 2.1.

The multiscale model we've used was initially introduced in our earlier work [49]. It was developed on a four-compartment volume conductor geometry. In this geometry, $\mathbf{A}$ represents the abdominal cavity with its boundary surface defined by $\partial\mathbf{A}$, outlining the abdomen. The myometrium is denoted by $\mathbf{M}$, and its external and internal boundary surfaces are denoted by $\partial\mathbf{M}$ and $\partial\mathbf{U}$, respectively. The volume $\mathbf{U}$ represents the space filled with amniotic fluid that exists between $\partial\mathbf{U}$ and the fetus-defined boundary $\partial\mathbf{F}$.

The electrical field is determined by the first three equations in Table 2.1, with the electrical potential $\phi(\boldsymbol{r}, t)$ generated by the myometrial current source density $\mathbf{J}\mathrm{s}(\boldsymbol{r}, t)$. This density, as per Ohm's law, is defined as the gradient of the action potential $v$ap.

The action potential v_{ap} is modeled as a function of the ionic current dynamics, $\boldsymbol{J}_{\text{ion}}\boldsymbol{(r, t)}$, and the stimulus current resulting from pacemakers, $\boldsymbol{J}_{\text{stim}}(\boldsymbol{r}, t)$. This modeling is achieved through the use of reaction-diffusion equations. Also, the anisotropic conductivities, $\boldsymbol{G}_i'$ and $\boldsymbol{G}_e'$, are taken into consideration along with the corresponding boundary condition equations provided in Table 2.1.

Through this modeling process, we've achieved a multiscale simulation that can capture the complex electrical activities in uterine contractions, providing us a way to study these phenomena in a comprehensive and realistic way.

Table 2.1: Equations of 3D COMSOL model [97, 49]

Electrical field	$\nabla \cdot \boldsymbol{G}_{\mathbf{A}}(\boldsymbol{r})\nabla\phi(\boldsymbol{r}, t) = 0, in \;\; \mathbf{A}$ $\nabla \cdot \boldsymbol{G}_{\mathbf{U}}(\boldsymbol{r})\nabla\phi(\boldsymbol{r}, t) = 0, in \;\; \mathbf{U}$ $\nabla \cdot \boldsymbol{G}_e'\nabla\phi_e(\boldsymbol{r}, t) = -\nabla \cdot \frac{\zeta}{\zeta+1}\boldsymbol{G}_e'\nabla v_{\text{ap}}(\boldsymbol{r}, t), in \; \mathbf{M}$
Source current density	$\boldsymbol{J}_{\text{s}}(\boldsymbol{r}, t) = -\zeta\boldsymbol{G}_e'\nabla v_{\text{ap}}(\boldsymbol{r}, t), in \;\; \mathbf{M}$
Action potential model	$\nabla \cdot \frac{\zeta}{\zeta+1}\boldsymbol{G}_e'\nabla v_{\text{ap}}(\boldsymbol{r}, t) = a_{\text{m}}(c_{\text{m}}\frac{\partial v_{\text{ap}}(\boldsymbol{r},t)}{\partial t} + \boldsymbol{J}_{\text{ion}}(\boldsymbol{r}, t) - \boldsymbol{J}_{\text{stim}}(\boldsymbol{r}, t)), in \;\; \mathbf{M}$ $\boldsymbol{J}_{\text{ion}}(\boldsymbol{r}, t) = \boldsymbol{J}_{\text{L-Ca}}(\boldsymbol{r}, t) + \boldsymbol{J}_{\text{T-Ca}}(\boldsymbol{r}, t) + \boldsymbol{J}_{\text{K1}}(\boldsymbol{r}, t) + \boldsymbol{J}_{\text{K2}}(\boldsymbol{r}, t) + \boldsymbol{J}_{\text{NSCC}}(\boldsymbol{r}, t)$ $\boldsymbol{J}_{\text{stim}}(\boldsymbol{r}, t) = \frac{1}{\epsilon_1}\sum_{i=1}^{N_{\text{p}}} v_i h_i(\boldsymbol{r}, t), in \;\; \mathbf{M}$
Boundary conditions	$\phi_{\text{e}}(\boldsymbol{r}, t) = \phi_{\mathbf{A}}(\boldsymbol{r}, \boldsymbol{t}), in \;\; \partial\mathbf{M}$ $\hat{\boldsymbol{n}}_{\mathbf{M}} \cdot (\boldsymbol{G}_i'\nabla\phi_{\text{i}}(\boldsymbol{r}, t) + \boldsymbol{G}_e'\nabla\phi_{\text{e}}(\boldsymbol{r}, t)) = \hat{\boldsymbol{n}}_{\mathbf{M}} \cdot \boldsymbol{G}_{\mathbf{A}}\nabla\phi_{\mathbf{A}}(\boldsymbol{r}, t), in \;\; \partial\mathbf{M}$ $\hat{\boldsymbol{n}}_{\mathbf{M}} \cdot \boldsymbol{G}_i'\nabla v_{\text{ap}}(\boldsymbol{r}, t) = 0, in \;\; \partial\mathbf{M}$ $\phi_{\text{e}}(\boldsymbol{r}, t) = \phi_{\mathbf{U}}(\boldsymbol{r}, t), in \;\; \partial\mathbf{U}$ $\hat{\boldsymbol{n}}_{\mathbf{U}} \cdot (\boldsymbol{G}_i'\nabla\phi_{\text{i}}(\boldsymbol{r}, t) + \boldsymbol{G}_e'\nabla\phi_{\text{e}}(\boldsymbol{r}, t)) = \hat{\boldsymbol{n}}_{\mathbf{U}} \cdot \boldsymbol{G}_{\mathbf{U}}\nabla\phi_{\mathbf{U}}(\boldsymbol{r}, t), in \;\; \partial\mathbf{U}$ $\hat{\boldsymbol{n}}_{\mathbf{U}} \cdot (\boldsymbol{G}_i'\nabla v_{\text{ap}}(\boldsymbol{r}, t) = 0, in \;\; \partial\mathbf{U}$ $\hat{\boldsymbol{n}}_{\mathbf{A}} \cdot (\boldsymbol{G}_{\mathbf{A}}\nabla\phi_{\mathbf{A}}(\boldsymbol{r}, t) = 0, in \;\; \partial\mathbf{A}$ $\hat{\boldsymbol{n}}_{\mathbf{F}} \cdot \boldsymbol{G}_{\mathbf{U}}\nabla\phi_{\mathbf{U}}(\boldsymbol{r}, t) = \lambda(\hat{\boldsymbol{n}}_{\mathbf{F}} \cdot \boldsymbol{G}_{\mathbf{F}}\nabla\phi_{\mathbf{F}}(\boldsymbol{r}, t)), in \;\; \partial\mathbf{F}$

The calculation of the action potential was performed using COMSOL Multiphysics version 5.3, executed on an Intel(R) Xeon(R) CPU E5-2650 v3 operating at 2.30 GHz, utilizing 20 cores across 2 sockets. The simulation utilized a fixed time step of 0.02 ms. During computation, the system consumed 59.33 GB of physical memory and 71.02 GB of virtual memory, with 1,928,485 degrees of freedom being accounted for.

Figure 2.8 presents the action potential propagation across a spherical model representing the uterine surface. Operating within a spherical volume conductor geometry, our simplified ionic channel model effectively imitates the patterns of the electrical field and the variations in the action potential. These results align well with the simulation results we obtained from MATLAB, and they are consistent with experimental data from the literature [11, 15].

These simulations provide a way to visualize the intricate and dynamic nature of action potential propagation in the uterus, which contributes to our understanding of the electrical phenomena involved in uterine contractions. This in turn could potentially assist in the development of new treatments or diagnostic tools for conditions related to uterine contractions.

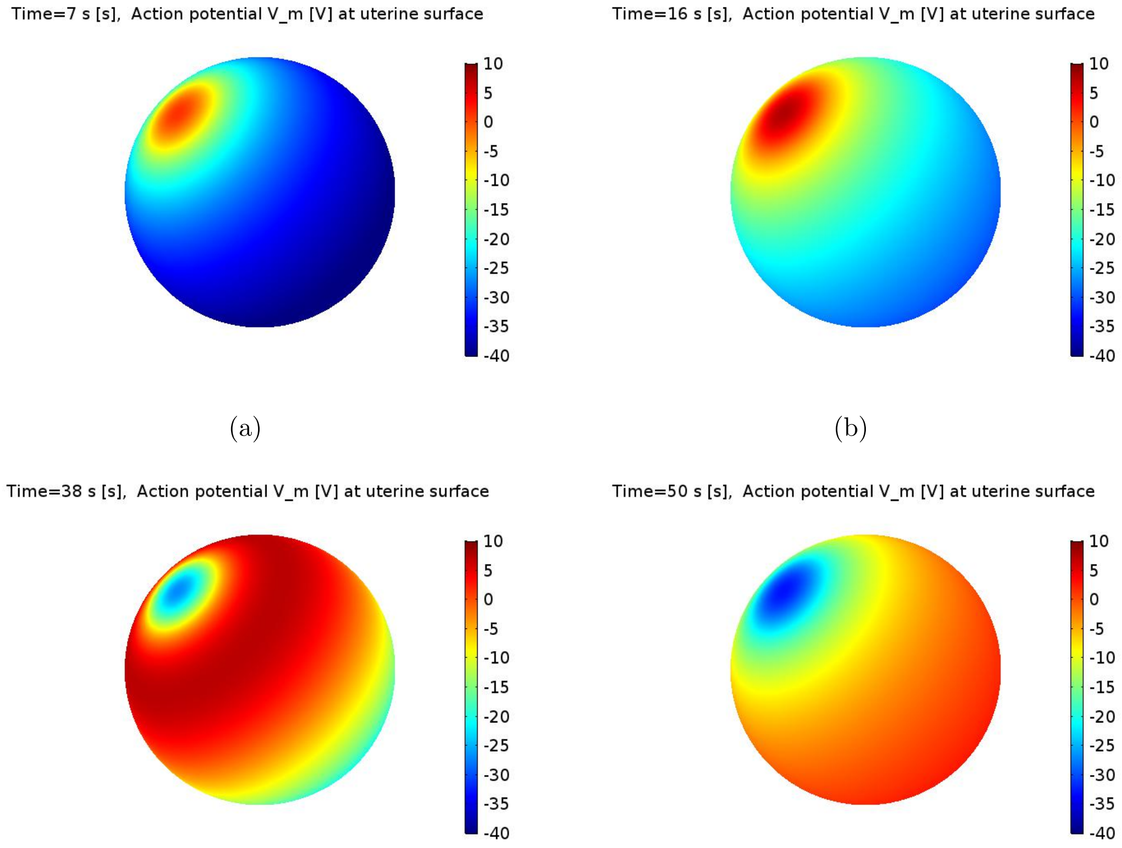

(a) (b) (c) (d)

Figure 2.8: 3D COMSOL simulation result of action potential at uterine surface.

2.4 Summary

This chapter has presented a comprehensive, robust framework of three interconnected models that simulate the biophysical dynamics of uterine contractions. The first is an ionic channel model that focuses on individual myocytes, which are crucial biological sensors within the myometrium. This model considers both electrochemical and bioelectrical properties, providing a highly detailed perspective on the cellular dynamics that underlie uterine activity.

The second is a mechanical model, which is predicated on the foundational principles laid down by the ionic channel model. This model introduces the element of cellular mechanical force, offering a macroscopic understanding of the physical movements during uterine contractions. It captures the force exerted by the individual myocytes and aggregates it to model the overall mechanical behavior of the uterus during contractions.

Lastly, we designed an oxytocin model that considers the hormone's role in modulating the dynamics of uterine contractions. Oxytocin, well-known for its role in childbirth, has significant impacts on both the electrical and mechanical properties of the uterus.

In addition to these complex models, we also developed a simplified version of the ionic channel model to facilitate large-scale simulations and analyses. The simplified model successfully replicates the biological and electrical activities associated with uterine contractions, demonstrating its utility and robustness.

In conclusion, our models accurately mimic the changes in electrical field patterns, the propagation of these patterns, and the generation of uterine mechanical force during contractions. They also effectively demonstrate the modulating influence of oxytocin on action potentials, cellular mechanical forces, and overall uterine contractions. These results strongly indicate that our models are capable of reproducing the key characteristics and dynamics of uterine contractions during pregnancy, providing a powerful tool for further study.

Chapter 3

Alya Purple: A Patient-Specific Multi-Scale, Multi-Physics Simulation of Human Uterine Peristalsis During the Menstrual Cycle[2]

The uterus undergoes frequent peristalsis driven by spontaneous mild contractions in the inner layer of the uterine smooth muscle. The peristaltic direction differs with the phase of the menstrual cycle and may be disrupted in disorders such as endometriosis, dysmenorrhea, and infertility. In the following chapter, we describe ”Alya Purple,” a computational framework for simulating human uterine peristalsis in three dimensions. Alya Purple incorporates electrical, mechanical, and structural data to create a patient-specific model. Additionally, Alya Purple simulates fluid flow within the uterus and thus can assess the movement of menstrual blood and sperm. Initial simulation data indicate that peristaltic waves moving in the cervix-to-fundus direction during menses can cause menstrual blood to enter the fallopian tubes and that this effect is enhanced in a model of the uterus in a patient with endometriosis. Additionally, our modeling shows that irregular peristalsis during the ovulatory phase can prevent sperm from reaching the fallopian tubes. Finally, in a modeling experiment, we show that applying an electrical stimulus to the fundus region of the uterus can counteract cervix-to-fundus peristaltic waves in the menses phase and thus prevent the movement of menstrual blood into the fallopian tubes. With further development, we anticipate that Alya Purple framework will support novel research into the electrophysiological and biomechanical aspects of uterine peristalsis and will allow patient-specific modeling of strategies to treat various menstrual disorders.

---

[2] This chapter is based on Lin, Yiqi, et al. ”Alya Purple: A Patient-Specific Multi-Scale, Multi-Physics Simulation of Human Uterine Peristalsis During the Menstrual Cycle” *ready to submit*

3.1 Overview of uterine peristalsis modeling

This section briefly describes the pre-existing uterine peristalsis models and then presents our approach to modeling.

3.1.1 Background

During the reproductive years of non-pregnant women, the uterus frequently undergoes peristalsis, manifested as mild spontaneous contractions within the inner layer of the uterine smooth muscle [48] [47]. Ultrasound studies reveal intriguing patterns in these waves of contractions: during the menses phase, they predominantly move from the fundus toward the cervix; conversely, during ovulation, these waves shift direction, moving from the cervix toward the fundus.

To quantify this process, uterine peristalsis imaging (UPI) was developed. This method uses MRI scans to map the uterus's geometry, then records the uterus's endogenous electrical activity using electrodes placed on the body's surface. These datasets are combined using UPI software, projecting the electrical activity onto the three-dimensional structure of the uterus. UPI studies of 17 participants have corroborated the previously observed patterns [84].

These patterns of uterine peristalsis are believed to have functional implications, and disruptions may contribute to pathologies [98] [6]. Waves moving from the fundus to the cervix likely help expel menstrual blood during menses. However, if these waves reverse direction frequently or strongly during this phase, they could cause retrograde menstruation and an increased risk of endometriosis [7][8][70]. During the ovulatory phase, waves moving from the cervix toward the fundus may help transport sperm toward the fallopian tubes, aiding in fertilization [48] [47].

3.1.2 Previous approaches

Multiscale models are powerful tools for investigating complex interactions at different levels within a system. Several researchers have developed such models to examine the uterus in three dimensions [49][97][91][93]. While generally focusing on the electrophysiological activities of uterine muscle cells, these models have often overlooked the mechanical deformations that the uterus undergoes during peristalsis. Moreover, these models have primarily relied on data from animal studies to establish quantitative features at the cellular level. This reliance could potentially limit their applicability to human uterine physiology, given the notable differences between species. Consequently, they might not accurately reflect the complex interplay of cellular and whole organ behavior that characterizes human uterine peristalsis.

When it comes to modeling the entire uterus, simplifications have been made that may detract from the model's precision. Some models depict the uterus as a sphere-like structure [49][97], a representation that oversimplifies the intricate and irregular geometry of the actual organ. Others are not tailored to a particular patient [91][93]. This lack of individual specificity can hamper the translation of findings from the computational model to clinical practice, where significant inter-individual differences in uterine morphology and physiology must be considered. Existing models also typically focus on the pregnant uterus, especially during the perinatal phase. However, the physiological mechanisms driving uterine contractions during pregnancy differ significantly from those governing uterine peristalsis throughout the menstrual cycle, and this focus may overlook important elements of non-pregnant uterine activity.

Interestingly, recent research suggests parallels between the initiation of uterine peristalsis and the initiation of mechanisms in the gastrointestinal system [25]. The interstitial cells of Cajal (ICCs) work in the gut as electrical pacemakers [71][1]. In the uterus, similar cells, termed interstitial Cajal-like cells (ICLCs) or myometrial Cajal-like cells, have been identified [16][40]. However, our nascent understanding of these cells and their electrophysiological function in the non-pregnant uterus is an exciting frontier in uterine physiology research.

Finally, the current models do not incorporate several crucial aspects of uterine peristalsis, such as fluid dynamics or the movement of particles. This oversight is significant, particularly in relation to processes such as menstrual flow and sperm transport.

3.1.3 Our approach

In this study, we developed a state-of-the-art, multi-scale, multi-physics whole uterus model, known as "Alya Purple," inspired by and evolving from Alya [37][36][10][79][80] and Alya Red[78]. The original Alya is a high-performance computational mechanics simulation system used predominantly in biomechanical research, and Alya Red is a computational heart model that is the current state-of-the-art in multi-scale heart simulations.

Alya Purple represents a significant enhancement over previous uterine models by integrating patient-specific anatomical data, diffusion magnetic resonance imaging (MRI) data, and uterine surface pacing data to simulate uterine peristalsis comprehensively and accurately. In the Alya Purple model, electrical propagation, which triggers mechanical deformation, is intertwined with fluid dynamics across cellular, tissue, and organ levels, faithfully recapitulating the multi-scale and multi-physics nature of uterine peristalsis.

This unique multi-scale and multi-physics approach enables non-invasive studies of uterine peristalsis patterns. The framework creates a comprehensive digital twin of the uterus, enabling a deep understanding of the intricate processes occurring during the menstrual cycle. This innovative method provides us with new ways to understand and potentially treat disorders linked with abnormal uterine peristalsis.

The impact of the Alya Purple extends beyond research and into clinical practice. By accurately and comprehensively elucidating uterine peristalsis, it is expected to enhance gynecological care and treatment planning. The ability to simulate uterine peristalsis based on patient-specific data could aid in the personalized management of several conditions linked with abnormal uterine contractions, such as infertility and endometriosis.

3.2 Alya Purple design and modeling

Alya Purple, built using insights from our uterine peristalsis imaging (UPI) findings, is an innovative, patient-specific model that simulates uterine peristalsis by integrating multiple physical processes, including electrical and mechanical processes and fluid dynamics. The inclusion and exclusion criteria for each patient group (normal and endometriosis) in the UPI studies, the consent process, and demographic, obstetric, and gynecologic history information for enrolled participants are discussed as follows.

The study, carried out under the purview of the Division of Reproductive Endocrinology & Infertility at Washington University School of Medicine, was approved by the Institutional Review Board of Washington University. Each participant was duly informed of the procedures and their potential implications, and their explicit written consent was obtained before initiation of the study.

The eligibility criteria for the study were carefully defined to enhance the validity and reliability of the findings. All potential participants were biologically female, aged between 18 and 37 years. For the group labeled 'normal,' the inclusion criterion was regular menstrual cycles, occurring every 24 to 35 days. For potential participants with a history of endometriosis, surgical confirmation of the diagnosis was required for inclusion.

Conversely, the study also defined a set of exclusion criteria: individuals who were post-menopausal, currently pregnant, or breastfeeding. Further, those with any form of uterine anomaly, a history of medication intake known to alter uterine contractility (such as magnesium, opioids, beta antagonists, and nifedipine), non-English speakers, and those with an abdominal circumference exceeding 55 cm were also excluded. The study additionally excluded individuals with contraindications to MRI, including the presence of a pacemaker or metal implants.

To refine the selection process further, potential participants for the 'normal' group were excluded if they reported or had documented histories of infertility, ovulatory dysfunction, or endometriosis. Similarly, the 'endometriosis' group excluded women currently using female birth control.

Out of the initial pool of potential participants, seventeen were classified as normal successfully completed the full course of the study, which involved longitudinal data acquisition and MRI study. Five additional patients with a confirmed diagnosis of endometriosis also completed the full course of he study. The demographic data, along with the obstetric and gynecologic histories of the enrolled participants, are presented in the UPI paper [84].

To capture the dynamics of uterine peristalsis across the menstrual cycle, each participant was subjected to UPI imaging during four distinct phases: menses, early proliferative, late proliferative (peri-ovulatory), and secretory. Blood samples were collected at each of these visits to determine the levels of estradiol, progesterone, and testosterone, and these measurements verified the phase of the menstrual cycle during each imaging session.

The following sections provide detailed descriptions of each component of Alya Purple.

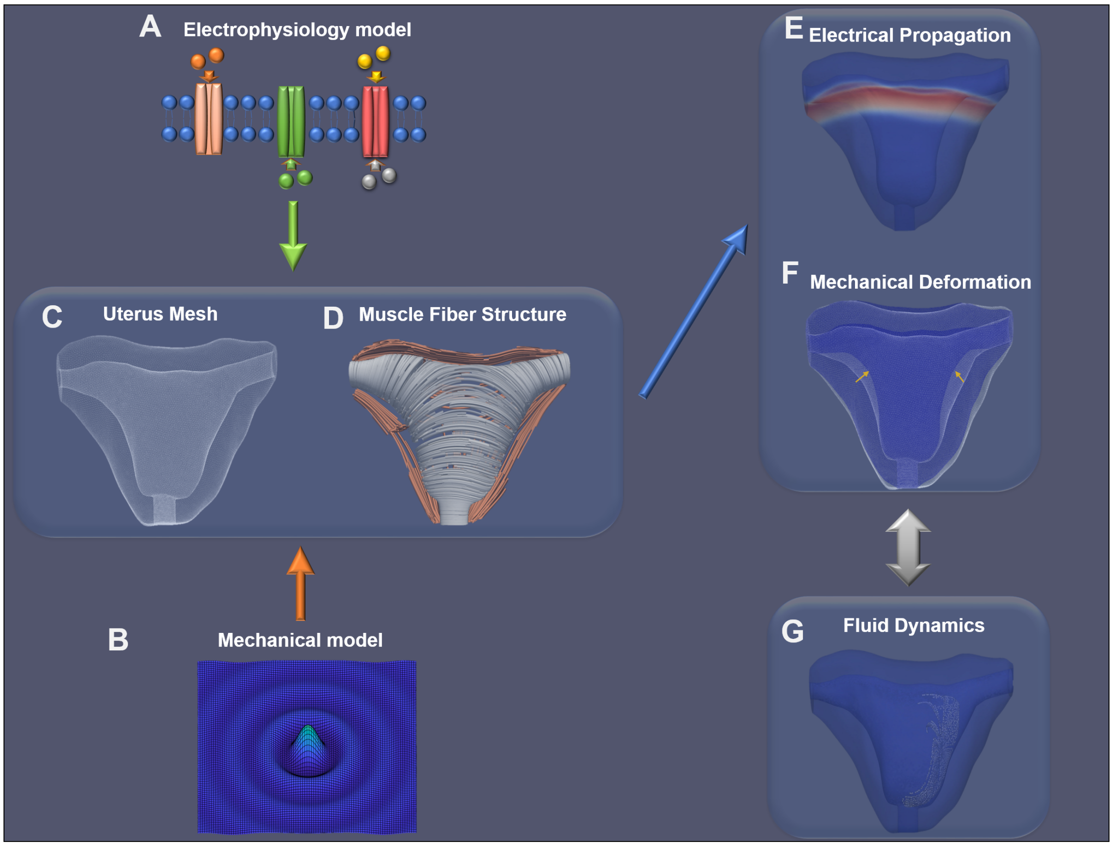

Figure 3.1: **Alya Purple flow chart.** A: The electrophysiological model, which represents the generation of action potentials from myocytes. B: The mechanical model, which illustrates the deformation of the uterus. C: Coupling of the electrophysiological (A) and mechanical (B) models applied to a meshed geometry of the uterus. D: The muscle fiber structure, which dictates the directional propagation of the coupled electrophysiological and mechanical models. E: Simulation of electrical propagation, depicting the electrical activities initiated by uterine peristalsis throughout the uterus. F: Simulation of mechanical deformation, observed as alterations in uterine shape. G: Simulated fluid dynamics, providing insight into the behavior and movement of particles within the uterus.

3.2.1 Electrophysiology model

The electrophysiology model, which simulates the electrical behaviors observed during uterine peristalsis, comprises two sub-components: electrical wave propagation and ionic current

Electrical wave propagation

The initiation of the propagation of an action potential along muscle fibers is precipitated by the depolarization of the cell membrane potential. This electrophysiological process is described by mathematical models that capture the intricate dynamics of electrical activation within the cellular system. For our analysis, we utilize a mathematical representation grounded in the modified FitzHugh-Nagumo model [68], a well-established model for action potential propagation.

The FitzHugh-Nagumo model provides a simplified yet effective approach to describe the complex behavior of electrical excitation and recovery in myocardial cells. Similarly, in the modeling of uterine electrophysiology, this model offers significant insights into the mechanisms that underlie the initiation and propagation of action potentials across muscle fibers.

It is essential to note that while the FitzHugh-Nagumo model has been widely used due to its simplicity and computational efficiency, it simplifies many physiological realities of the underlying biological systems. Nevertheless, this model captures the essential dynamics required for the present study, providing a foundation for our description of the propagation of the electrical activation potential, ϕ, in uterine muscle tissue.

In our study, the propagation of electrical activation potential is denoted by the variable ϕ:

$$\frac{\partial \phi}{\partial t} = \frac{\partial}{\partial x_i}(D_{ij}\frac{\partial \phi}{\partial x_j}) + L(\phi). \tag{3.1}$$

The diffusion term is governed by the diffusion tensor D_{ij}, which reflects the muscle fiber orientation (discussed in section 2.5) in the myometrium. $L(\phi)$ represents the total ionic current across the membrane.

Ionic current

No comprehensive ionic channel model has been described to represent the electromyographic activities generated by ICLCs in the non-pregnant uterus [25][16][40]. Thus, we constructed a model that emulates slow wave propagation patterns analogous to those observed in the gastrointestinal system [1]. This resemblance is not surprising, given the presence of ICLCs, which serve a similar role to the Interstitial Cells of Cajal (ICCs) in the gut, acting as electrical pacemakers.

We employed the modified FitzHugh-Nagumo model [68] [24], a simplified but insightful mathematical construct, to represent the electrical activities initiated by ICLCs. This model was chosen for its capacity to effectively simulate electrical wave propagation after pacing the uterus at an initiation area, as determined by UPI.

Within the FitzHugh-Nagumo model, a fast variable, ϕ, denotes the primary signal responsible for initiating action potentials. In addition, a slow variable, v, expresses the recovery rate, characterizing the time-dependent relaxation phase of the action potential. Together, these variables capture the complex spatiotemporal dynamics of uterine electrical activity and provide a comprehensive description of the electromyographic activities instigated by ICLCs in a non-pregnant uterus:

$$\begin{aligned} \frac{\partial \phi}{\partial t} &= \nabla \cdot D \nabla \phi + c_1 \phi(\phi - a)(1 - \phi) - c_2 \phi v \\ \frac{\partial v}{\partial t} &= b(\phi - dv). \end{aligned} \tag{3.2}$$

Here, ϕ denotes the electrical potential and v denotes the recovery rate. The fast variable, ϕ, fits the Hodgkin-Huxley type kinetics, whereas the slow variable, v, fits an exponential relaxation process. D denotes the diffusion tensor, and a,b,c_1,c_2, and d are membrane parameters that determine the shape of the action potential pulse.

3.2.2 Mechanical model

The mechanical deformation model in this study represents a compressible solid in three-dimensional elements. The material model used is based on the principles of hyperelasticity, a nonlinear relationship between stress and strain that is a characteristic feature of biological tissues.

To accurately capture the mechanical deformation, we have previously used a transversely isotropic variant of the Holzapfel-Ogden material model [35]. The Holzapfel-Ogden model is an established material model extensively utilized in biomechanical simulations due to its ability to capture the mechanical characteristics of soft tissues with a high degree of accuracy [50]. Our variant of this model effectively captures the inherent complexities of uterine tissue, including its nonlinear stress-strain relationship and anisotropic behavior. The ensuing sections provide a more detailed exposition of the Holzapfel-Ogden material model and how it is implemented within our framework.

Mechanical deformation

Within a fixed reference configuration of a uterus, the position vector is represented by X_I, whereas in a deformed configuration, it is x_i. Linear momentum balance in the fixed reference configuration is articulated by a total Lagrangian finite element formulation via the following governing equations:

$$\rho \frac{\partial^2 u_i}{\partial t^2} = \frac{\partial P_{iJ}}{\partial X_J} + \rho B_i, \tag{3.3}$$

where ρ denotes the organ's initial density, B_i is the uterine mechanical force, and P_{iJ} denotes the first Piola–Kirchhoff stress tensor.

The deformation gradient tensor relates both measures:

$$F_{iJ} = \frac{\partial x_i}{\partial X_J} = \delta_{iJ} + \frac{\partial u_i}{\partial X_J}, \tag{3.4}$$

where the displacement is $u_i = x_i$-X_I

Mechanical stress

The Piola–Kirchhoff stress tensor, P_{iJ}, defines the Cauchy stress as:

$$\sigma = J^{-1} \boldsymbol{P} \boldsymbol{F}^T, \tag{3.5}$$

where J is the determinant of the deformation gradient $J = \det(\mathrm{F})$.

In uterine tissue, it is posited that stress results from the interplay of both passive and active stress components [38].

$$\sigma = \sigma_{\text{pas}} + \sigma_{\text{act}}(\lambda, [\text{Ca}^{2+}])\text{f} \otimes \text{f}. \tag{3.6}$$

The passive component of stress in the uterine tissue is construed as a slightly compressible invariant-type material, utilizing a transverse isotropic exponential strain energy function. This constitutive relationship illustrates the material's response to exerted loads, dictated by the material's innate structure. The strain energy function establishes a correlation between the Cauchy stress, σ, the right Cauchy-Green deformation tensor, b, and the strain invariants[35] [49]:

$$J\sigma_{\text{pas}} = (ae^{b(I_1-3)} - a)\boldsymbol{b} + 2a_f(I_4-1)e^{b_f(I_4-1)^2}\boldsymbol{f} \otimes \boldsymbol{f} + K(J-1)\,\mathbf{I}. \tag{3.7}$$

The strain invariants, I_1 and I_4, correspond respectively to the non-collagenous material and the stiffness of muscle fibers. The right Cauchy–Green deformation $\boldsymbol{b}$ is equal to $\boldsymbol{F}$ times $\boldsymbol{F}^T$. The parameters a, b, a_f, and b_f are determined experimentally to describe the strain energy, and K designates the compressibility of the material. The vector $\boldsymbol{f} = \boldsymbol{F}\boldsymbol{f}_0$ delineates the direction of the fibers, which influences the propagation of electrophysiology; $\boldsymbol{f}_0$ is the mean fiber orientation.

3.2.3 Coupling model

We adopted the excitation-contraction coupling model developed by Hunter and McCulloch [39]. This model is predicated on the principle that active stress, a quantification of mechanical force per unit area of tissue, is produced in the direction of the muscle fibers immediately following a waveform generated by electrical activation. A pivotal element in the genesis of this active stress is the transient surge in calcium levels within myometrial cells.

Calcium ions are integral to the production of mechanical force in biological tissues. To represent this key factor within our model, we make use of a parameterizable calcium transient waveform [63]. The resulting function offers a robust method for triggering active tension within the myometrial tissues (detailed in equation 3.8). Thus, our computational model effectively represents the intertwined processes of electrical excitation and subsequent mechanical contraction in the uterus.

$$\sigma_{\mathrm{act}} = \frac{[\mathrm{Ca}^{2+}]^{\mathrm{n}}}{[\mathrm{Ca}^{2+}]^{\mathrm{n}} + \mathrm{C_{50}}^{\mathrm{n}}} \sigma_{\max}(1 + \beta(\lambda_f - 1)), \tag{3.8}$$

where C_{50} is the calcium concentration for 50 % of $\sigma_{\max}$, n is a coefficient that controls the shape of the curve, $\sigma_{\max}$ is the maximum tensile stress generated at the maximum extension ratio $\lambda = 1$, and β is a parameter that scales the active stress produced.

This waveform is coupled to the electrophysiology model following the activation wavefront, whereby the electrical activation triggers the calcium transient[39]. We detect the zero-crossing of voltage which triggers the calcium function. Here, we calculate the time-dependent intracellular calcium concentration as follows:

$$[\mathrm{Ca}^{2+}](\mathrm{t_{loc}}) = [\mathrm{Ca}^{2+}]_{\max}(\mathrm{t_{loc}}/\tau_{\mathrm{Ca}})\mathrm{e}^{1-\mathrm{t_{loc}}/\tau\mathrm{Ca}}, \tag{3.9}$$

where τ_{Ca} is the time to achieve the maximum calcium concentration value $[\mathrm{Ca}^{2+}]_{\max}$ and t_{loc} is the local activation time triggered by the electrical wave propagation.

3.2.4 Fluid model

For the fluid dynamics simulations in the uterus, Alya Purple relies on Computational Fluid Dynamics (CFD) [72]. CFD, a branch of fluid mechanics that uses numerical analysis and algorithms to solve and analyze problems involving fluid flows, is particularly applicable here given the fluid-structure interactions happening within the uterus.

The fluid flow within the uterus is governed by the Navier-Stokes equations, which are a set of nonlinear partial differential equations describing the motion of viscous fluid substances. As the uterus's internal environment consists of an incompressible Newtonian fluid, these equations are well suited for our simulation requirements.

Moreover, due to the dynamic, deformable nature of the uterus, a fixed Eulerian mesh (a grid system where the fluid moves through the stationary grid points) might not accurately capture the intricacies of the fluid flow. Hence, we utilize an arbitrary Lagrangian-Eulerian

(ALE) scheme. This scheme allows the computational mesh to move and deform with the uterus, ensuring the physiological and biomechanical accuracies of the simulations.

In an ALE scheme, the mesh is neither entirely Eulerian (where the mesh does not move with the fluid) nor Lagrangian (where the mesh moves with the fluid). Because the mesh can move arbitrarily, it can accurately simulate complex fluid-structure interactions, like those found in the uterus during peristalsis. In an ALE scheme, the mesh can deform based on the electro-mechanic activity of the uterus and the motion of the fluid. The incompressible flow assumption is valid for low-speed flow, which is typically the case in physiological processes.

Here, the flow equations are

$$\begin{gathered}\rho^f \frac{\partial v_i}{\partial t} + \rho^f (v_j - v_j^m) \frac{\partial v_i}{\partial x_j} + \frac{\partial}{\partial x_j}[p\delta_{ij} - \mu(\frac{\partial v_i}{\partial x_j} + \frac{\partial v_j}{\partial x_i})] = \rho^f f_i \\ \frac{\partial v_i}{\partial x_i} = 0,\end{gathered} \tag{3.10}$$

where μ is the viscosity, ρ^f is the fluid density, v_i is the velocity, p is the mechanical pressure, f_i is the volumetric force term, and $v_j^m$is the mesh velocity.

3.2.5 Geometry and microstructure

In this study, the uterus geometry was generated using patient-specific MRI data obtained with a Siemens Vida 3T MRI Scanner. The anatomical MR images were used to segment in detail various anatomical features, such as the uterine surface, cervix, and uterine cavity (Figure 3.2A). However, due to the large pixel size of the segmented MR images, interpolation was required to bridge the gap between each layer of data. To ensure a more accurate and realistic geometry, we manually smoothed the uterine anatomy.

Following the segmentation and smoothing, we created a tetrahedral mesh on the myometrium of the uterus, derived directly from the segmented images (Figure 3.2B). In forming this mesh, we made sure to include at least four transmural elements so we could apply the boundary conditions to the external muscles. The modified Fitzhugh-Nagumo model used in this study, known for its lack of a steep slope, allowed a low mesh resolution, so the edge length of the elements was approximately 1 millimeter. The same mesh was employed for calculating both the electrophysiology propagation and the mechanical deformation, contributing to the consistency of our computational model.

The overall model's realism and accuracy were partially determined by the representations of the myometrial fibers' orientations. To this end, we adopted a detailed process where diffusion tensor imaging (DTI)-derived data was refined and interpolated with the meshed uterus geometry. DTI, a type of MRI technique, can determine the primary orientation of uterine myometrial fibers. Because patient movement can create errors during imaging, we carefully segmented the uterus boundary on the DTI images. We then used the uterus boundary segmentations to align each frame of the MR image, further refining the fiber orientations.

Drawing upon previous studies [86], the DTI-derived data was further refined and smoothed according to the primary fiber direction in each area of the myometrium. The final representation of the fiber orientation is illustrated in Figure 3.2C. The successful integration of these complex processes demonstrates the robustness of our modeling approach and its potential to contribute significantly to uterine physiology and pathology.

Since uterine peristalsis primarily originates and propagates inside the inner one-third of the myometrium, in this study, we set the inner one-third region as having low electrical resistance, and the outer two-thirds as having high resistance, constraining electrical activities to the inner one-third. In Figure 3.2C, fibers in different directions represent different conductivities: a longitudinal fiber represents a high conductivity muscle, and a circular fiber represents a low conductivity muscle.

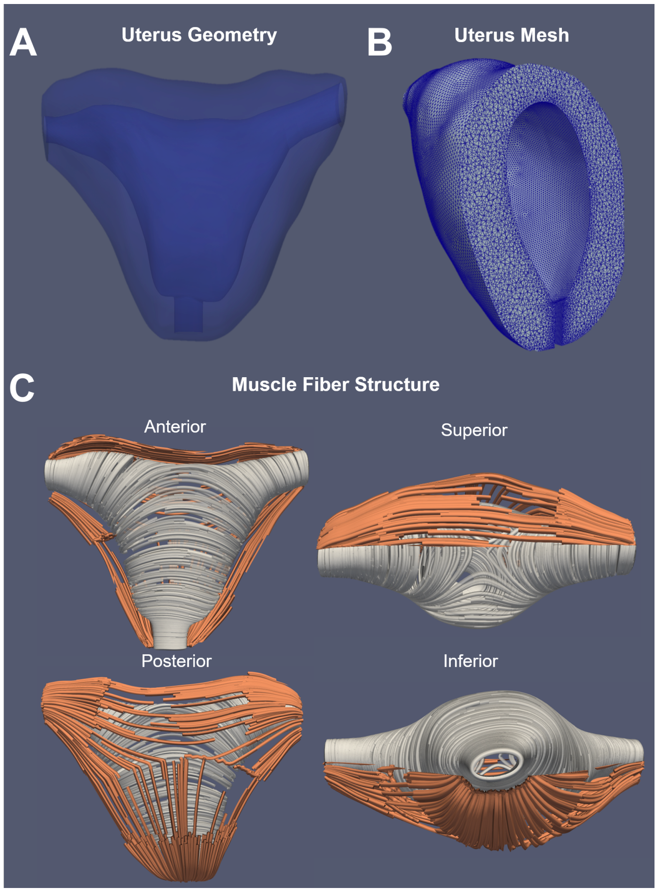

Figure 3.2: **Uterine geometry and microstructure**. (A) Whole uterus segmentation of a uterine MRI image, including the uterus surface, cervix, and myometrium. (B) Uterus mesh result. (C) Refined muscle fiber structure (white: circular fibers on the inner layer, orange: longitudinal fibers on the outer layer).

3.3 Simulation examples and discussion

3.3.1 Simulation of uterine peristalsis during the menses phase in participants with normal menstrual cycles

To apply Alya Purple in simulating uterine peristalsis waves in a patient exhibiting a normal menstrual cycle, we initially derived the uterine geometry from MRI data. Concurrently, DTI data was used to refine the uterine fiber structure (Figure 3.2).

With the anatomical model ready, we used the patient's UPI data collected during the menses phase as the foundation for simulations. This data, as reported in a recent publication [84], tied our simulations to the patient's specific physiology.

In the simulation, as depicted in Figure 3.3A, the Alya Purple framework represents a typical peristalsis wave during the menses phase of a menstrual cycle. This wave originates near the fundus (upper part of the uterus) and the left fallopian tube, then moves towards the cervix (lower part of the uterus).

To better visualize the fluid dynamics, menstrual blood is represented by three sets of red particles within the uterine cavity –on the left side, the right side, and the area around the fundus. The Alya Purple simulation demonstrates that the peristaltic wave, through the action potential it generates, can effectively push some of these particles towards the cervix, eventually causing them to exit the uterus at approximately the 3.00 seconds mark in the simulation.

Figure 3.3B explores the movement of menstrual blood during a peristalsis wave that starts at the cervix and travels towards the fundus. This pattern is often observed in cases of "retrograde menstruation", where menstrual blood is propelled in a direction opposite to the usual cervix-exiting flow. The simulation demonstrates that the first electrical wave initiates at the cervical area, which subsequently triggers corresponding mechanical deformation within the uterine muscle tissue.

As a result of the first cervix-to-fundus peristalsis wave (spanning 1.00 to 6.00 seconds in Figure 3.3B), a portion of the menstrual blood is moved towards the part of the uterus close to the fallopian tubes. Upon the initiation of subsequent peristalsis, some of the menstrual

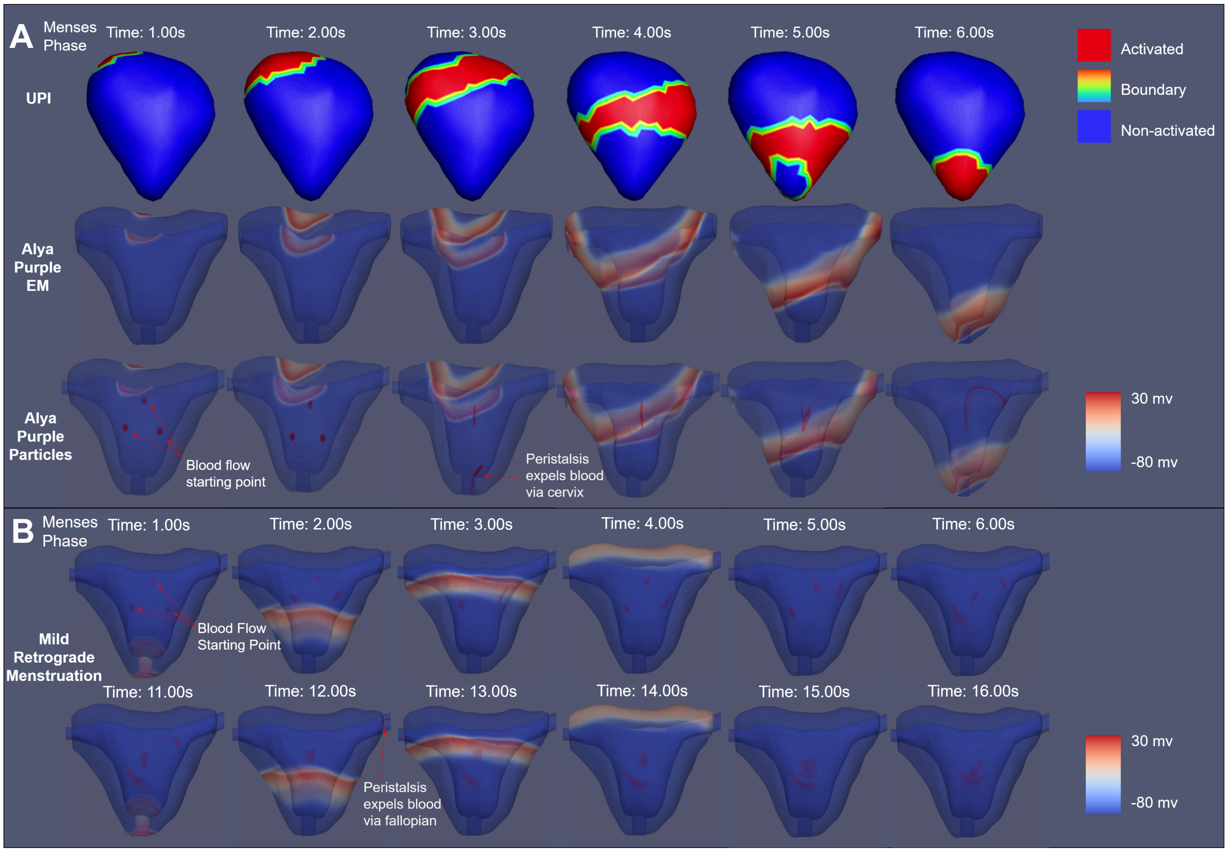

Figure 3.3: **UPI and Alya Purple results for a normal group patient during the menses phase.** (A) Comparative UPI and Alya purple results. (B) Alya Purple simulation of mild retrograde menstruation. Red shows the activated regions of the uterus, and blue indicates the resting regions. Alya Purple EM (electromechanical) results showing six frames of electro-mechanical propagation of uterine peristalsis compared with UPI results. Alya Purple particle results illustrate the simulation coupled with fluid dynamics. Here, the red particles indicate the menstrual blood from three different areas of the uterus (left, right, and fundus).

blood is propelled into the fallopian tube, occurring at approximately 12.00 seconds in the simulation.

3.3.2 Simulation of uterine peristalsis during the ovulatory phase in patients with normal menstrual cycles

Subsequently, the Alya Purple framework was employed to simulate uterine peristalsis during the ovulatory phase in women with normal menstrual cycles. Figure 3.4A demonstrates a characteristic cervix-to-fundus uterine peristalsis wave, which was recorded through UPI. The Alya Purple simulation, mirroring the dynamics captured in the UPI data, shows that the peristalsis wave travels in a similar direction and at a comparable speed.

To investigate the influence of a cervix-to-fundus peristalsis wave on sperm movement following intercourse, white particles were introduced into the cervix region in the Alya Purple model to simulate uterine insemination. The sperm, driven by the peristalsis wave, moved upwards from the cervix towards the left fallopian tube. Quantitative analysis (Figure 4C) revealed that, following three instances of cervix-to-fundus peristalsis waves, about 77.46% of the sperm had successfully reached the fallopian tube.

We also utilized Alya Purple to simulate instances of irregular uterine peristalsis during the ovulatory phase in a patient with normal menstrual cycles. In the scenario depicted in Figure 3.4B, two consecutive peristalsis waves move from the right side of the uterus to the left. This unusual wave pattern, deviating from the typical cervix-to-fundus flow, seemed to hinder efficient sperm transportation towards the fallopian tubes. A quantitative analysis (Figure 3.4D) demonstrated that, after experiencing three right-to-left peristalsis waves, only 41.93% of the sperm managed to reach the end of the fallopian tubes closest to the uterus.

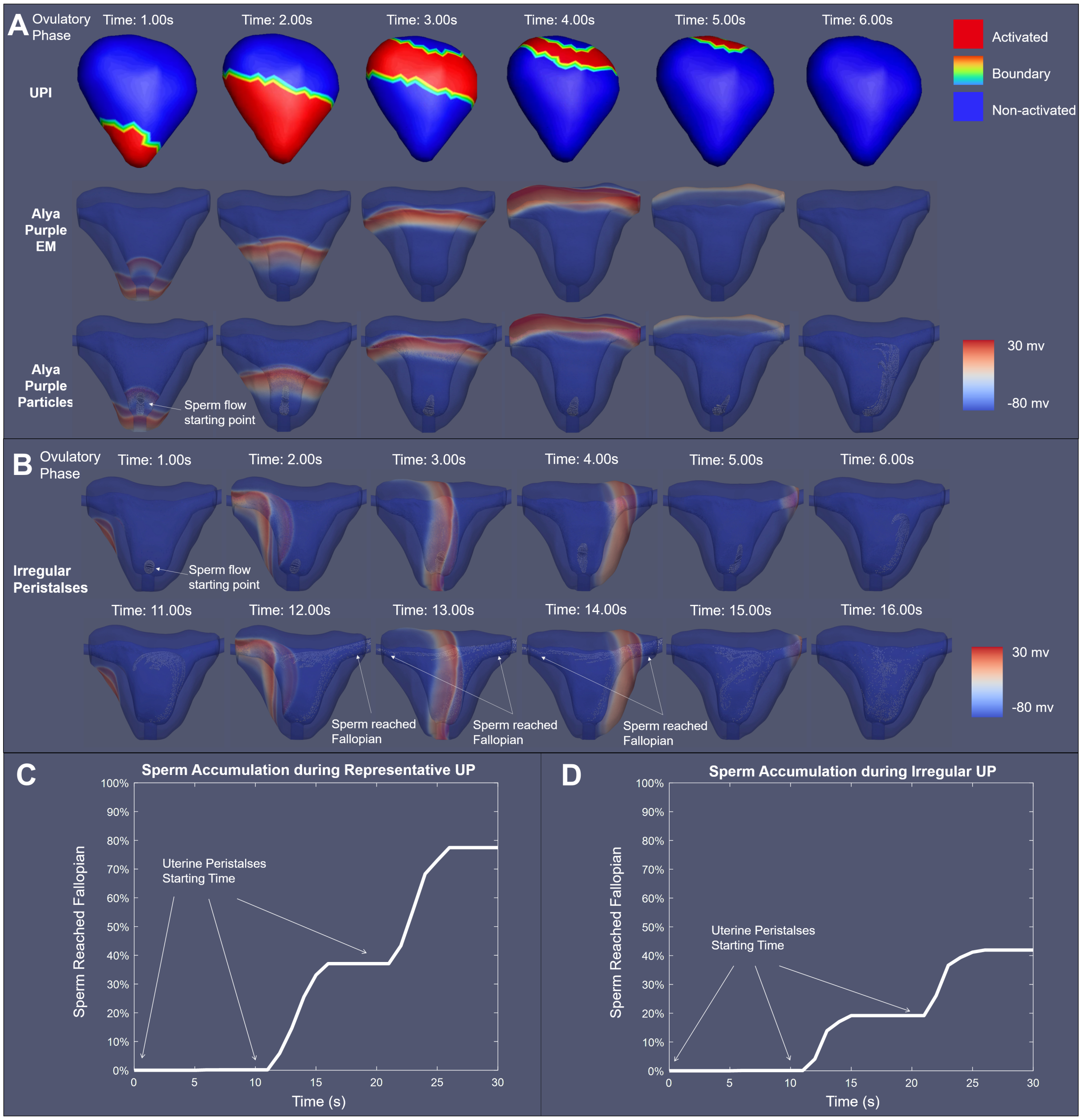

Figure 3.4: **UPI and Alya Purple results for a normal group patient during the ovulatory phase.** (A) Comparative UPI and Alya purple results. (B) Alya Purple simulation of irregular peristalses. (C) The number of sperm reaching the end of the fallopian tubes during representative regular peristalses from the cervix to the fundus and (D) during irregular peristalses, from the patient's right to their left. In A and B, the red indicates the activated regions of the uterus and blue indicates the resting regions. Alya Purple EM (electromechanical) results for 6 frames of electro-mechanical propagation of uterine peristalses, compared with UPI results in the top row. Alya Purple Particles results illustrate the simulation coupled with fluid dynamics and particles. Here, the white particles inside the uterus indicate sperm which propagate from the cervix.

3.3.3 Simulation of uterine peristalsis in the menses phase of a patient with endometriosis

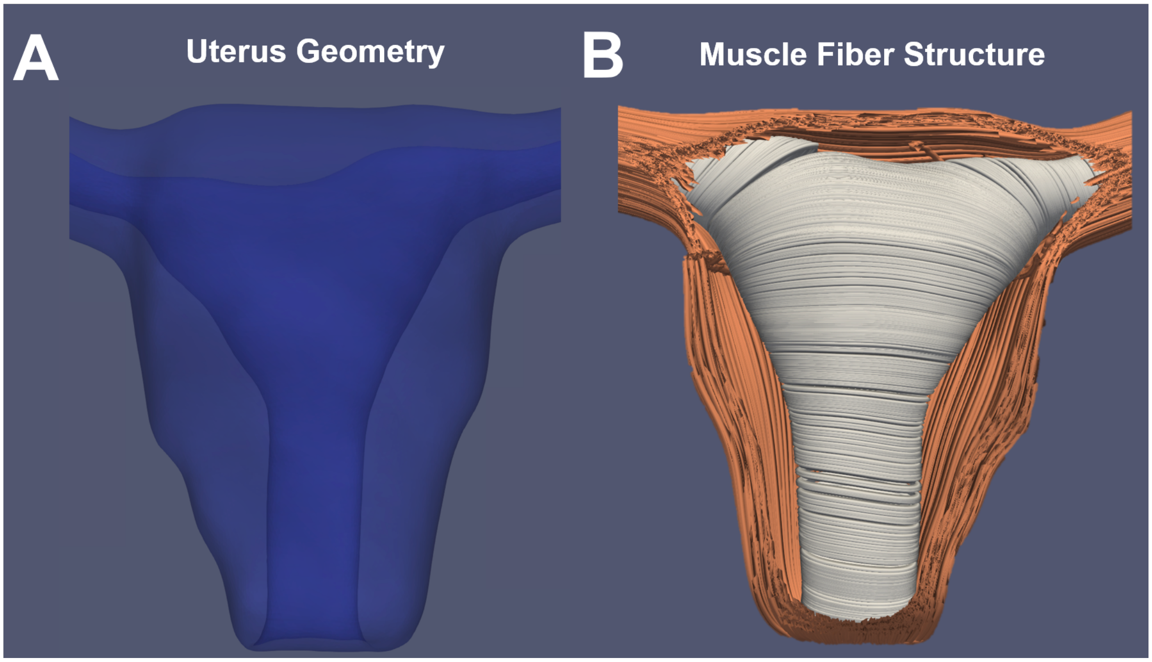

Figure 3.5: **Uterine geometry and microstructure of an endometriosis patient.** (A) Uterine geometry segmented from uterine MR image of an endometriosis patient. (B) Refined uterine muscle fiber structure of an endometriosis patient (white, circular fibers in the inner layer; orange, longitudinal fibers in the outer layer).

The Alya Purple framework was used to simulate uterine peristalsis during the menses phase in a patient diagnosed with endometriosis. First, the uterine geometry was generated from MRI data, then the fiber structure was refined with the help of DTI data (Figure 3.5).

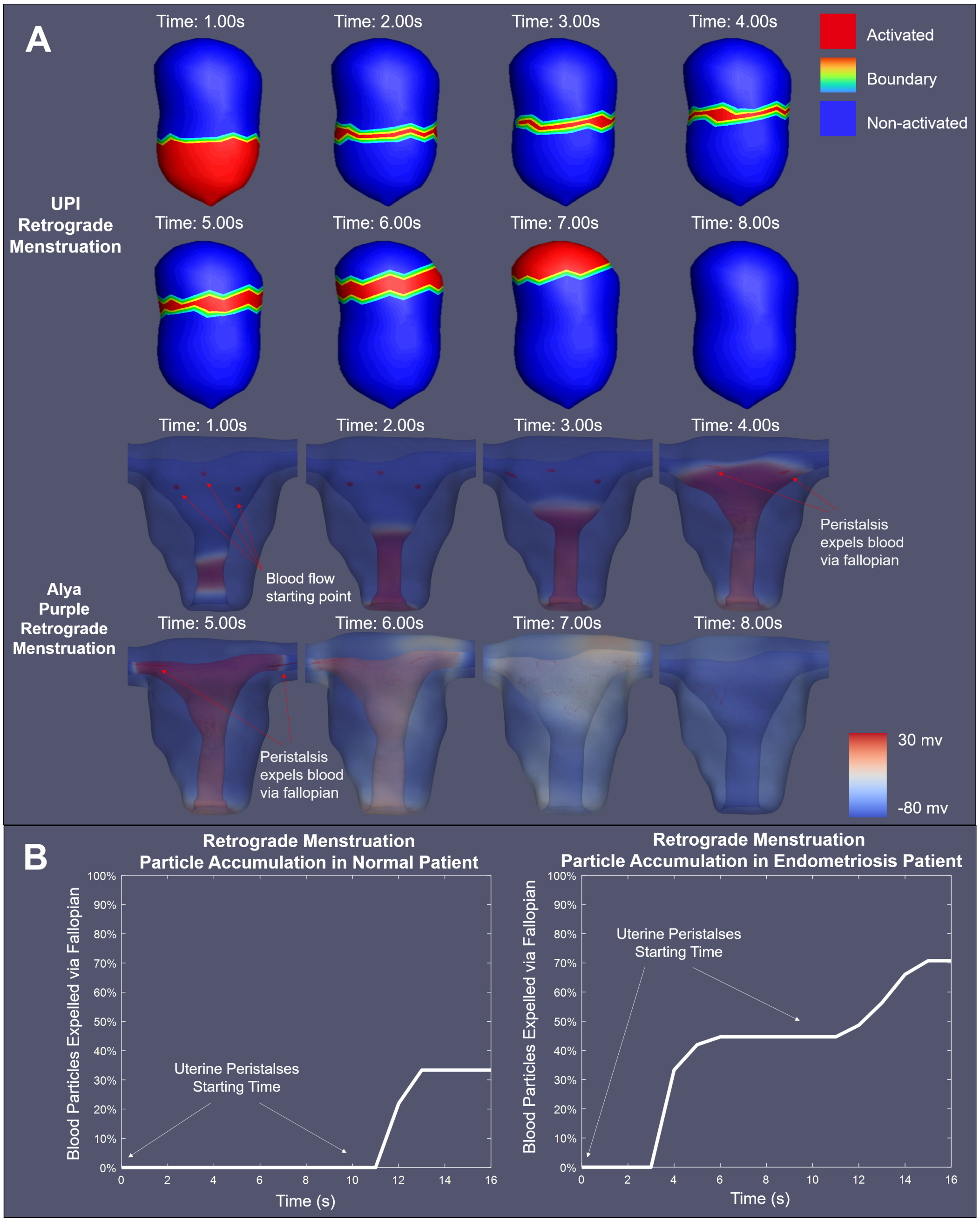

Figure 3.6: **UPI and Alya Purple results for an endometriosis group patient during the menses phase.** (A) Comparative UPI and Alya purple results for retrograde menstruation. (B) The number of blood particles expelled via fallopian tubes during retrograde menstruation in a normal patient (B, left) and an endometriosis patient (B, right). In A and B, red indicates the activated regions of the uterus, and the blue shows resting regions. Red particles indicate menstrual blood from three different areas of the uterus (left, right, and fundus).

Based on the UPI results shown in Figure 3.6A, an electrical stimulus was applied to the cervical area of the model, followed by mechanical deformation in accordance with the electrical propagation pattern. To represent menstrual blood within the uterine cavity, red particles were introduced at the left, right, and fundus. As the cervix-to-fundus peristalsis wave progressed, the Alya Purple simulation showed that some of the red particles were pushed into both fallopian tubes.

We then quantitatively analyzed the simulated blood flow following the cervix-to-fundus peristalsis waves, both in the patient with normal menstrual cycles (Figure 3.3B) and in the patient diagnosed with endometriosis (Figure 3.6A). To conduct this analysis, 1000 particles were placed in three distinct areas within the uterus to represent menstrual blood in the left, right, and fundus regions of the uterus. After two peristalsis waves, 33.34% of the particles in the simulation of the patient with normal menstrual cycles reached the fallopian tubes. However, in the simulation of the patient with endometriosis, a significantly higher proportion (70.72%) of the particles were propelled into the fallopian tubes (Figure 3.6B). This finding suggests a potential correlation between the incidence of endometriosis and increased retrograde menstruation.

3.3.4 Modeling the effects of electrical pacing to reverse the peristaltic wave direction

In the concluding phase of the study, Alya Purple was used to simulate a situation where a pacing signal is applied to the fundal side of the uterus in a patient exhibiting strong cervix-to-fundus peristalsis during the menses phase.

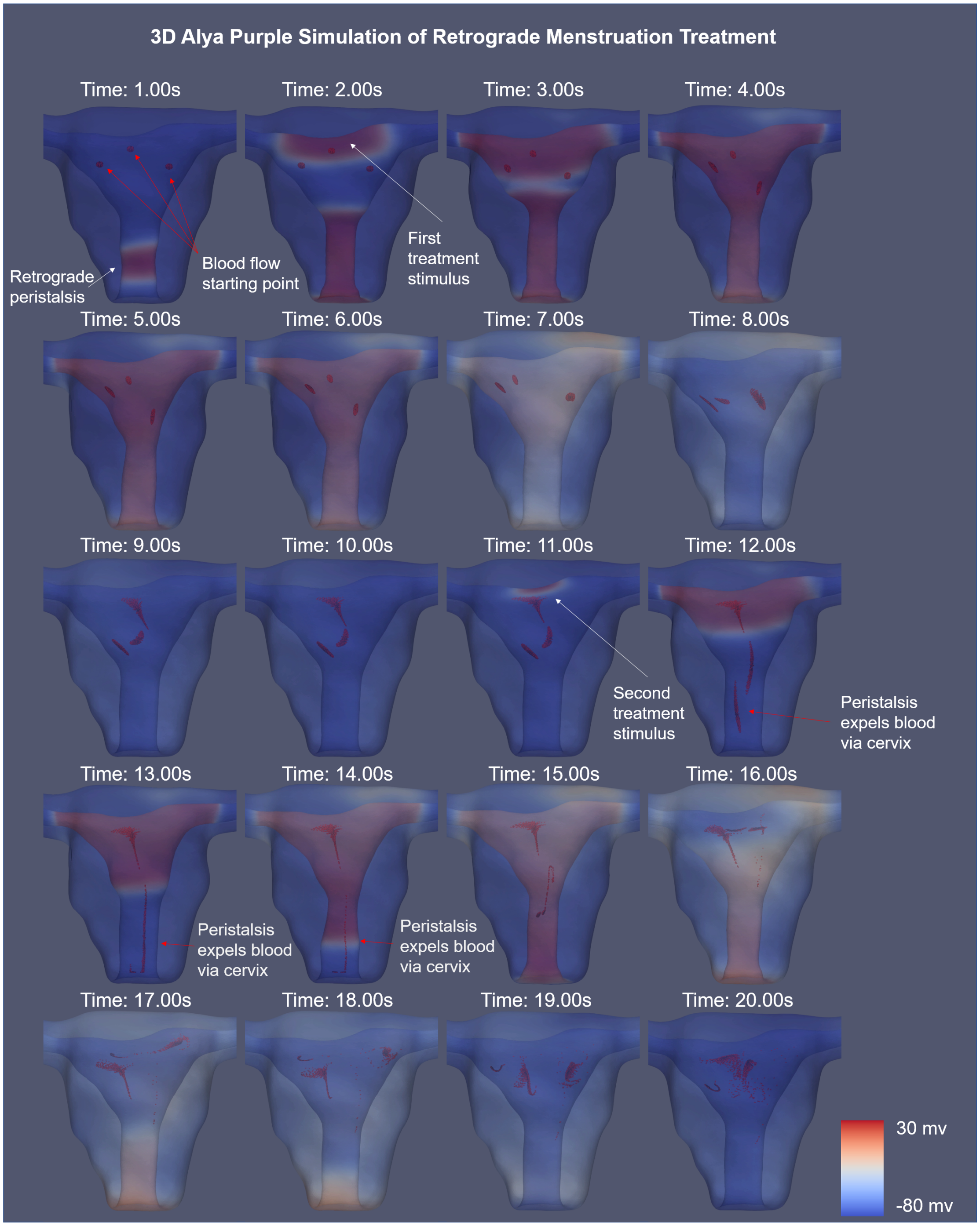

Figure 3.7: **Virtual intervention placed to neutralize the retrograde menstruation.** Twenty chronological frames illustrating the propagation of a uterine peristaltic wave that causes retrograde menstruation, along with two treatment stimuli applied one second and ten seconds after the retrogression is detected. Here, red particles represent menstrual blood originating from three distinct regions of the uterus (left, right, and fundus). The red arrows in the first frame highlight the initial locations of these particles, and the white arrows in frames 2 and 11 indicate the initiation point of treatment stimuli.

The reference simulation for this analysis, shown in Figure 3.6A, was the untreated control case. The pacing scenario was commenced at 2.00 seconds into the simulation shown in Figure 3.7. At this point, a pacemaker, located at the fundus of the uterus, was activated one second after a peristalsis wave began at the cervix, which caused a new wave to propagate from the fundus towards the cervix.

As a result of this stimulus, the simulated menstrual blood, represented by red particles, remained within the uterus instead of being propelled into the fallopian tubes. Subsequently, a second pacing signal was introduced at 11.00 seconds, which triggered another peristalsis wave moving towards the cervix and led to the expulsion of blood particles through the cervix, beginning at 13.00 seconds.

Together, the two pacing stimuli resulted in the cervical expulsion of 28% of the simulated menstrual blood. This finding suggests the potential of using targeted pacing interventions to manage the progression of conditions like endometriosis by modulating the direction and pattern of uterine peristalsis.

3.4 Summary

This study demonstrated Alya Purple's ability to simulate diverse patterns of uterine peristalsis, focusing specifically on the menses and ovulatory phases of the menstrual cycle. The results of these simulations align consistently with those observed in UPI data. Alya Purple effectively combines the principles of electrophysiology, mechanobiology, and fluid dynamics to provide a multi-dimensional perspective on uterine function and to simulate the movement of both menstrual blood and sperm within the uterus.

The model revealed that, during the menstrual phase in a healthy patient, peristalsis from the cervix toward the fundus can induce mild retrograde menstruation, displacing menstrual blood into the fallopian tube and potentially into the abdomen. This retrograde menstruation was enhanced in a model of a patient with endometriosis, and it could contribute to the development of endometriosis.

Further simulations of the ovulatory cycle provided insights into the effect of uterine peristalsis on the movement of sperm toward the fallopian tube. Our results suggest that irregular uterine peristalsis can significantly decrease the proportion of sperm reaching the fallopian tube, potentially explaining subfertility or infertility in patients with irregular menstrual cycles.

Finally, we explored the potential use of Alya Purple to model the effects of electrical pacing as a means to manipulate the direction of uterine peristalsis. This simulation provided theoretical evidence that uterine pacing might be a viable strategy for managing conditions like irregular menstruation, endometriosis, and infertility. However, this strategy is still far from clinical feasibility. Its perceived tolerability and safety from the facts that most patients are not conscious of their frequent uterine peristalsis, and the pacing signals are relatively mild.

In conclusion, the Alya Purple 3D human uterine contraction simulation framework is a novel tool for studying the complex interplay of electrophysiology, mechanobiology, and fluid dynamics in uterine peristalsis.

Chapter 4

Application of Alya Purple to Human Uterine Contractions during Pregnancy

During pregnancy and labor, the rate and strength of uterine contractions can prompt obstetrical interventions, and contractions in preterm patients may indicate preterm labor. Previously, our lab developed the electromyometrial imaging system (EMMI) to gather clinical data and measure the electrical activity of patients' uterine contractions during pregnancy [82]. However, there is limited research on virtual three-dimensional frameworks to simulate the uterine contractions during pregnancy.

As discussed in Chapter 4, we have developed a new framework for simulating human uterine peristalsis during the menstrual cycle, named ”Alya Purple”. In this chapter, based on patient-specific EMMI, we use Alya Purple to simulate human uterine contractions in 3D during pregnancy. This new system provides a virtual way to integrate clinical data and simulate the electrical transmembrane potential propagation driving uterine contractions in a heterogeneous patient population. The system can simulate mechanical deformation and fluid dynamics in synchrony with electrical propagation to reveal the mechanism of human uterine contractions. Our results demonstrate the underlying biology of human uterine contractions and provide clinical insight into normal labor progression. We anticipate that our system will support novel research in the electrophysiological and biomechanical aspects of pregnancy.

4.1 Difference between Alya Purple applications in electromyometrial imaging (EMMI) and uterine peristalsis imaging (UPI)

Although EMMI and UPI studies both consider uterine activity, EMMI focuses on pregnancy and UPI focuses on the menstrual cycle. The nonpregnant uterus undergoes four distinct menstrual phases: menstruation, the follicular phase, ovulation, and the luteal phase. These sequential events give rise to variations in uterine peristalsis, which are the main focus of a UPI study. In general, a single peristaltic wave lasts between 3 to 20 seconds, although this duration may vary among individuals.

On the other hand, EMMI is used in studying labor and delivery, where uterine contractions crucially facilitate the expulsion of the fetus. Compared to uterine peristalsis, these contractions are significantly longer, ranging from 30 to 80 seconds. The primary aim of an EMMI study is to understand the directional and other electrical properties of these contractions and how they correlate with the progression of labor.

Another difference between these two studies is the structural geometry of the uterus in pregnant and nonpregnant states. As we discuss in the next section, to tailor predictive models to the specific context of study - menstrual cycles or labor and delivery - these geometric differences must be taken into account.

4.2 Geometry and microstructure of the pregnant uterus

Pregnant and non-pregnant uteruses have quite different geometries. During gestation, to accommodate the growing fetus and placenta, the uterus expands to more than 100 times its original size, creating a complex environment within. In this study, to construct a model of this environment, we employ patient-specific MRI data acquired with a Siemens Vida 3T MRI Scanner.

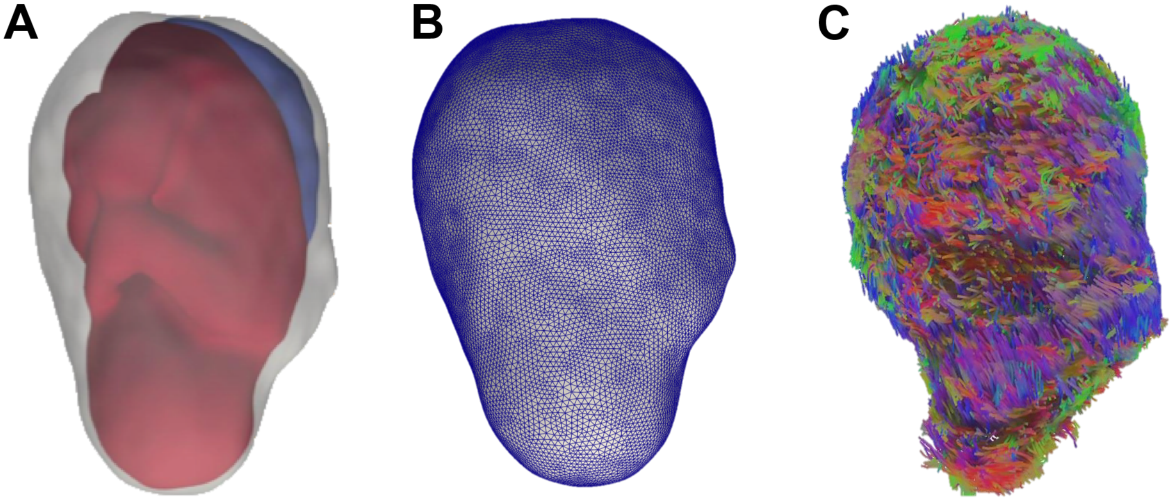

Figure 4.1: **Uterus geometry and microstructure of a pregnant patient.** (A) Uterus geometry segmented from uterus MR images of a pregnant patient (grey, uterus boundary; red, fetus; blue, placenta). (B) Uterus surface mesh result. (C) Uterus muscle fiber structure from DTI image.

Derived from the MRI data, anatomical images were utilized to create a detailed segmentation of various features, including the uterine surface, cervix, fetus, and placenta (Figure 4.1A). Due to the inherently large pixel size of the segmented MR images, interpolation was used to bridge between each layer of data. For a more realistic geometry, we manually smoothed the image.

Following the segmentation and smoothing, we created a tetrahedral mesh on the myometrium of the uterus, directly derived from the segmented uterine surface images (Figure 4.1B). Due to the distinctive electrical and mechanical properties of the amniotic fluid, fetus, and placenta, we simplified the model by calculating only the uterus surface.

In constructing the mesh, we included at least four transmural elements, needed for applying boundary conditions to the external muscles. The modified Fitzhugh- Nagumo model, known for its relatively flat slope, indicated that the mesh resolution need not be exceptionally high. Thus, the edge length of the elements was approximately 1 millimeter. For consistency, the same mesh was employed for both electrophysiology propagation and mechanical deformation computations. Accurate knowledge of the muscle fiber orientation is needed to precisely simulate the electrophysiological propagation and mechanical behavior of the uterus, so we used diffusion tensor imaging (DTI) to extract reliable muscle fiber orientation data.

To compensate for the inherent inaccuracies arising from patient movement during the imaging procedure, we applied image registration techniques. This involved segmenting the uterus boundary on multiple DTI images, each with a different b-value, an MRI parameter that reflects the sensitivity of the imaging to the diffusion of water molecules. By registering these segmented images, we could generate a more realistic representation of the muscle fiber orientation.

Despite better fiber orientation data obtained through this process, the data representation still appears complex due to the intricate structure of the uterine muscle. However, we chose not to further smooth or simplify this data to avoid loss of detail and maintain the integrity and authenticity of the original data. Future work may look into ways of improving the quality of the fiber orientation data while preserving its complexity, which would allow for even more accurate simulations of uterine peristalsis and related phenomena.

4.3 Simulation results and discussion

In this section, we present simulation results for uterine contractions in pregnancy generated by the Alya Purple computational framework using the new geometry and microstructure of pregnant uterus. Additionally, we demonstrate the model's ability to recreate contractions as imaged by EMMI in patient examinations.

4.3.1 Alya Purple's ability to reproduce uterine contraction during pregnancy

Alya Purple's ability to simulate the initiation and propagation of uterine contractions from single or dual pacing sites provides a powerful tool for understanding the dynamics of labor. As depicted in Figure 4.2A, a typical contraction begins at the fundus and propagates toward the cervix, mimicking the natural process that aids in childbirth. This pacing from the fundus, where the electrical wave travels throughout the uterus, can allow researchers and clinicians to predict and analyze various patterns of labor, possibly leading to more effective intervention strategies when labor does not progress as expected.

Figure 4.2B illustrates Alya Purple's ability to simulate two successive contractions, each originating from a different point. Initially the uterus is stimulated at the fundus, followed by a secondary stimulus on the lateral area of the uterine surface after 6 seconds. This sequence generates two action potentials from these distinct pacing sites, propagating in different directions. Approximately 13 seconds later, these separate action potentials converge at the fallopian tube region, combining to form a single new action potential wave that continues to propagate across the uterine surface and eventually reaches the cervix. This ability to model complex scenarios could prove invaluable in the study of complicated labor patterns.

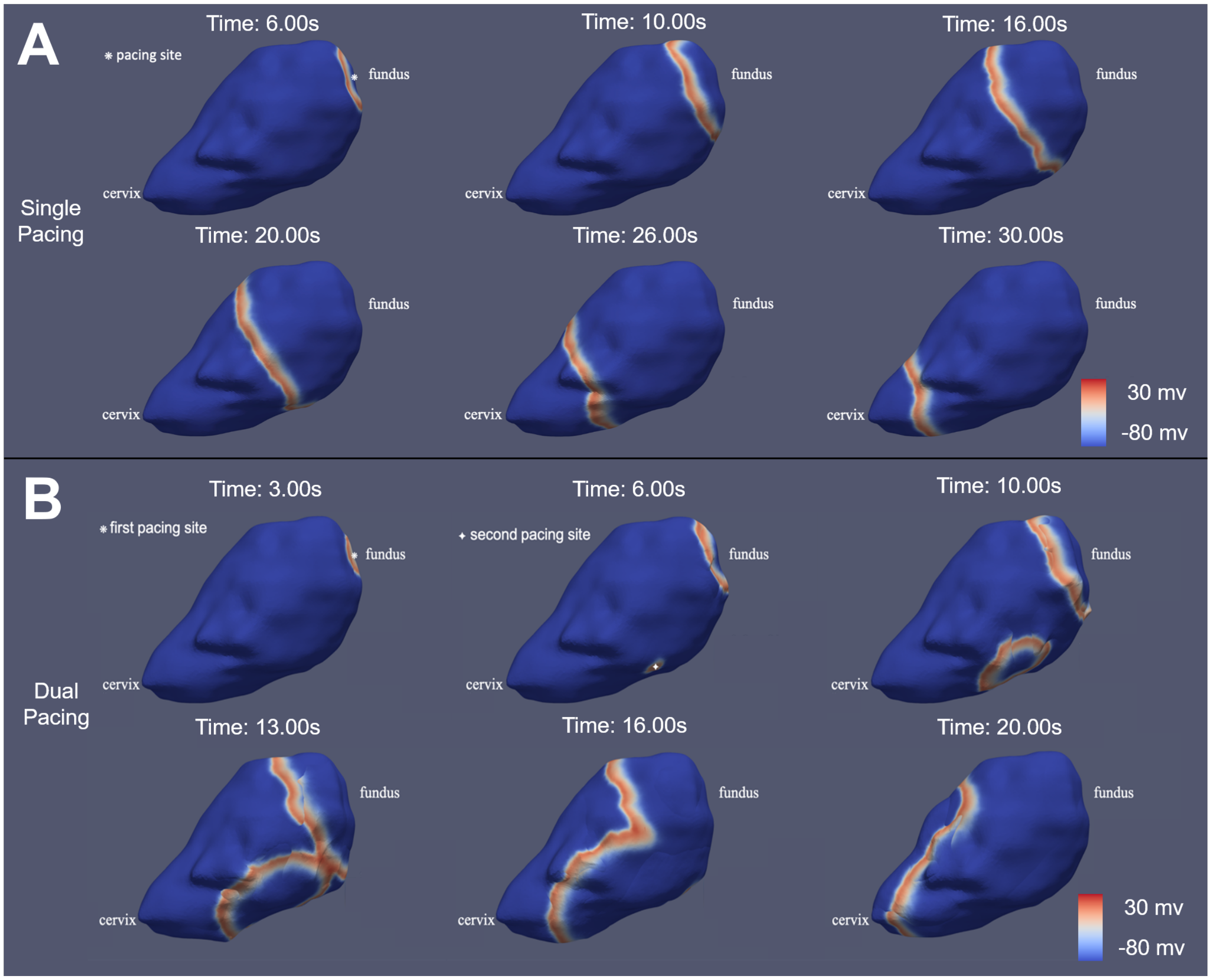

Figure 4.2: **Alya Purple results for pregnant patients.** Six successive frames imaging the electrical propagation of uterine contractions. (A) Electrical propagation result for a single pacing site. (B)Electrical propagation result for dual pacing sites.

These pacing scenarios are representative of the typical uterine contraction patterns observed in our EMMI study, and we proceeded to compare them with our empirical data from patient uterine contractions as imaged by EMMI.

4.3.2 Alya Purple simulation results compared with EMMI results

The efficacy of Alya Purple in replicating the intricate dynamics of uterine contractions is further highlighted when the simulations are compared with actual patient data from EMMI, as shown in Figure 4.3.

For this patient, Figure 4.3 shows two distinct representative contractions. The initial contraction is initiated from a single pacing site near the right fallopian tube, with the action potential propagating towards the cervix. The comparison of our simulation results (bottom row) with the empirical human contraction data (top row) in Figure 4.3 indicates a high degree of accuracy in the Alya Purple model's reproduction and evaluation of this contraction.

Figure 4.3B presents a slightly more complex scenario, where the uterine contraction is initiated from two separate pacing sites near both the left and right fallopian tube regions. In this case, the propagation and interaction of the two action potential waves is slower. Notably, the active area of the uterus at the pacing time (indicated in red) was smaller than that of the first contraction, with a narrower wave bandwidth and slower propagation speed for the action potential.

The concurrence of the simulation and human experimental results gives us confidence in the predictive capability of this model. It successfully captured both the simple contraction pattern initiated near the right fallopian tube and the more complex scenario involving two pacing sites near the left and right fallopian tube regions.

The simulations also allowed for careful analysis of various characteristics of the contractions, such as the active area of the uterus at the pacing time, the bandwidth of the action potential wave, and the speed of propagation. These parameters could potentially help clinicians in understanding why certain labors progress slowly and in devising strategies to facilitate them.

The time to complete a single simulation, approximately 6 hours on a server with 96 cores, points to the computational intensity of these simulations. However, considering the value of the intricate details these simulations can capture and the potential insights they can provide into the mechanics of childbirth, the computational demand is justified.

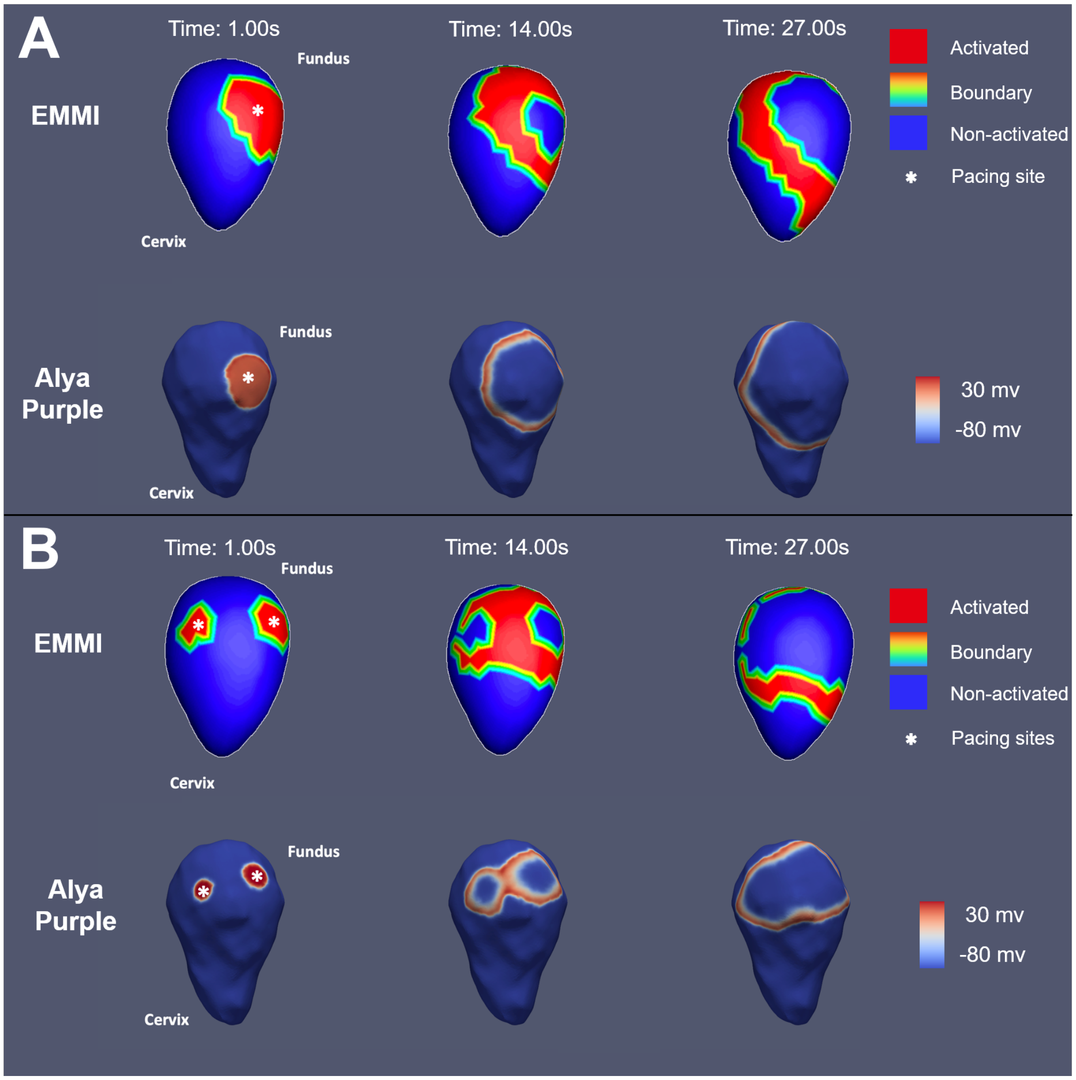

Figure 4.3: Three sequential frames of **EMMI and Alya Purple results for a pregnant patient.** (A) Comparative EMMI and Alya purple results for a single pacing site. (B) Comparative EMMI and Alya purple results for dual pacing sites. Here, red shows the activated parts of the uterus, and blue shows the resting area.

4.4 Summary

Because uterine contractions during pregnancy affect both childbirth complications and preterm labor, it is crucial to grasp their underlying electrophysiology and mechanobiology. Irregular uterine contractions can result in labor discomfort and potential complications for both mother and baby. To decode the mechanisms of these issues, we have created the Alya Purple 3D human uterine contraction simulation framework, which integrates multi-scale, multi-physics data derived from noninvasive medical imaging techniques. This virtual platform places the patient at the center of both diagnostic and therapeutic strategies for labor-related complications.

Alya Purple can simulate diverse uterine contraction patterns, reflecting different pacing sites. We have demonstrated the use of Alya Purple in simulations that map uterine contractions at various pacing sites, such as a single pacing site and dual pacing sites which start at different areas of the uterus. The simulation outcomes present distinct propagation patterns that mirror alterations in uterine conditions, aligning with clinical observations. These findings highlight Alya Purple's ability to simulate diverse uterine contraction patterns and its potential for revealing the mechanisms contributing to complications during childbirth.

In essence, the Alya Purple 3D human uterine contraction simulation framework offers a powerful tool for exploring the electrophysiology and mechanobiology of uterine contractions. Its ability to simulate diverse uterine contraction patterns and to validate simulation results with experimental data can help to elucidate the mechanisms of labor complications.

Chapter 5

Conclusion and Future work

5.1 Conclusion

Throughout these chapters, the intricacies of uterine contractions and peristalsis during both pregnancy and menstrual cycles have been elucidated using advanced simulation frameworks. Initially, a modeling approach was introduced to accurately capture the biophysical dynamics of uterine contractions during pregnancy, emphasizing the roles of ionic channels, mechanical force, and oxytocin effects. Subsequently, the Alya Purple simulation framework was highlighted, demonstrating its ability to depict the diverse patterns of uterine peristalsis across different menstrual cycle stages. The findings underscored the potential implications of irregular peristalsis on conditions such as retrograde menstruation and endometriosis. Moreover, the potential of electrical pacing as a therapeutic strategy was explored for various uterine conditions. Finally, the versatility and patient-centric nature of the Alya Purple 3D human uterine contraction simulation framework was emphasized, with its potential for simulating a broad spectrum of contraction patterns and pacing sites. This ability to capture, simulate, and consequently interpret multi-scale and multi-physics uterine activities represents a substantial step forward in our understanding of the uterus's electrophysiology and mechanobiology. With these tools described in this dissertation, we move closer to more comprehensive diagnostic and therapeutic strategies that could improve outcomes and quality of life for those facing pregnancy-related complications and menstrual irregularities.

5.2 Future work

Our ongoing and future research will enhance the precision and comprehensiveness of our uterine models. We will refine the accuracy of our ionic channel model by integrating a more extensive set of laboratory data, notably data from multiple ionic channels in the human uterus. The integration of this model into our multiscale 3D human uterus simulation will be paramount in understanding the propagation of ionic currents. It will offer insights into their response to hormonal shifts, such as alterations in oxytocin levels, and their subsequent impacts on uterine pressure. Concurrently, efforts will be channeled into constructing a predictive model to estimate delivery time, aiming to provide valuable tools for the early diagnosis of preterm labor.

Parallel to these pursuits, future endeavors will be geared towards constructing more holistic models that accurately map particle trajectories throughout the menstrual cycle. Recognizing the intricacies of the female reproductive anatomy, we will incorporate models of the uterus, cervix, and fallopian tubes that are anatomically precise, thus boosting the reliability of simulations. Simulating diverse, patient-specific uterine peristalsis patterns will aid in assessing innovative interventions like electrical pacing. The overarching aspiration with Alya Purple is not just to gain a deeper understanding of conditions such as endometriosis but also to pioneer and test patient-centric therapeutic strategies.

In line with these initiatives, our future research on the pregnant uterus will focus on uterine contraction simulations with a more realistic model geometry. By leveraging the insights from non-pregnant uterus peristalsis studies, we envision creating sophisticated models that emulate the intricacies of uterine contractions during pregnancy. Such models hold the promise of unveiling the nuanced mechanisms underpinning contractions and providing clinicians with enhanced tools for pregnancy management.

References

[1] M. A. Ahmed and R. Jung. Modeling of slow waves in the stomach. In *Encyclopedia of Computational Neuroscience*, pages 2064–2072. Springer, 2022.

[2] C. V. Ananth, C. V. Ananth, and A. M. Vintzileos. Epidemiology of preterm birth and its clinical subtypes. *The Journal of Maternal-Fetal & Neonatal Medicine*, 19(12):773–782, 2006.

[3] F. Arias. Pharmacology of oxytocin and prostaglandins. *Clinical Obstetrics and Gynecology*, 43(3):455–468, 2000.

[4] S. Arrowsmith and S. Wray. Oxytocin: its mechanism of action and receptor signaling in the myometrium. *Journal of neuroendocrinology*, 26(6):356–369, 2014.

[5] P. S. Buford. *Human uterine smooth muscle single cell model.* PhD thesis, University of Arkansas at Little Rock, Little Rock, AR, USA, 2007.

[6] C. Bulletti and D. De Ziegler. Uterine contractility and embryo implantation. *Current Opinion in Obstetrics and Gynecology*, 17(3):265–276, 2005.

[7] C. Bulletti, D. De Ziegler, V. Polli, E. Del Ferro, S. Palini, and C. Flamigni. Characteristics of uterine contractility during menses in women with mild to moderate endometriosis. *Fertility and sterility*, 77(6):1156–1161, 2002.

[8] C. Bulletti, D. DE ZIEGLER, S. Rossi, V. Polli, M. Massoneau, E. Rossi, A. Albonetti, V. Negrini, and C. Flamigni. Abnormal uterine contractility in nonpregnant women. *Annals of the New York Academy of Sciences*, 828(1):223–229, 1997.

[9] T. Burdyga, S. Wray, and K. Noble. In situ calcium signaling: no calcium sparks detected in rat myometrium. *Annals of the New York Academy of Sciences*, 1101(1):85–96, 2007.

[10] E. Casoni, A. Jérusalem, C. Samaniego, B. Eguzkitza, P. Lafortune, D. Tjahjanto, X. Sáez, G. Houzeaux, and M. Vázquez. Alya: computational solid mechanics for supercomputers. *Archives of Computational Methods in Engineering*, 22:557–576, 2015.

[11] R. Casteels and H. Kuriyama. Membrane potential and ionic content in pregnant and non-pregnant rat myometrium. *The Journal of physiology*, 177(2):263–287, 1965.

[12] W. A. Catterall. Voltage-gated calcium channels. *Cold Spring Harbor perspectives in biology*, 3(8):a003947, 2011.

[13] T. Chard and J. G. Grudzinskas. *The uterus.* Cambridge University Press, 1994.

[14] S. Degani, Z. Leibovitz, I. Shapiro, R. Gonen, and G. Ohel. Myometrial thickness in pregnancy: longitudinal sonographic study. *Journal of ultrasound in medicine*, 17(10):661–665, 1998.

[15] J. Dolenšek, D. Špelič, M. Klemen, B. Žalik, M. Gosak, M. Rupnik, and A. Stožer. Membrane potential and calcium dynamics in beta cells from mouse pancreas tissue slices: theory, experimentation, and analysis. *Sensors*, 15(11):27393–27419, 2015.

[16] M. Domino, B. Pawlinski, M. Gajewska, T. Jasinski, M. Sady, and Z. Gajewski. Uterine emg activity in the non-pregnant sow during estrous cycle. *BMC veterinary research*, 14:1–9, 2018.

[17] S. el Manouni el Hassani, H. Niemarkt, H. Said, D. Berkhout, A. van Kaam, R. van Lingen, M. Benninga, N. de Boer, and T. de Meij. Fecal volatile organic compounds in preterm infants are influenced by enteral feeding composition. *Sensors*, 18(9):3037, 2018.

[18] B. Ermentrout. *Simulating, analyzing, and animating dynamical systems: a guide to XPPAUT for researchers and students*, volume 14. Siam, 2002.

[19] D. Escalona-Vargas, R. B. Govindan, A. Furdea, P. Murphy, C. L. Lowery, and H. Eswaran. Characterizing the propagation of uterine electrophysiological signals recorded with a multi-sensor abdominal array in term pregnancies. *PloS one*, 10(10):e0140894, 2015.

[20] J. Espinoza, J. P. Kusanovic, C. J. Kim, Y. M. Kim, J.-S. Kim, S. S. Hassan, F. Gotsch, L. F. Gonçalves, O. Erez, L. Friel, et al. An episode of preterm labor is a risk factor for the birth of a small-for-gestational-age neonate. *American journal of obstetrics and gynecology*, 196(6):574–e1, 2007.

[21] H. Eswaran, H. Preissl, J. D. Wilson, P. Murphy, S. E. Robinson, and C. L. Lowery. First magnetomyographic recordings of uterine activity with spatial-temporal information with a 151-channel sensor array. *American journal of obstetrics and gynecology*, 187(1):145–151, 2002.

[22] T. Y. Euliano, M. T. Nguyen, S. Darmanjian, S. P. McGorray, N. Euliano, A. Onkala, and A. R. Gregg. Monitoring uterine activity during labor: a comparison of 3 methods. *American journal of obstetrics and gynecology*, 208(1):66–e1, 2013.

[23] J. J. Ferreira, A. Butler, R. Stewart, A. L. Gonzalez-Cota, P. Lybaert, C. Amazu, E. L. Reinl, M. Wakle-Prabagaran, L. Salkoff, S. K. England, et al. Oxytocin can regulate myometrial smooth muscle excitability by inhibiting the na+-activated k+ channel, slo2. 1. *The Journal of physiology*, 597(1):137–149, 2019.

[24] R. FitzHugh. Impulses and physiological states in theoretical models of nerve membrane. *Biophysical journal*, 1(6):445–466, 1961.

[25] A. S. Garrett, S. A. Means, M. W. Roesler, K. J. Miller, L. K. Cheng, and A. R. Clark. Modeling and experimental approaches for elucidating multi-scale uterine smooth muscle electro-and mechano-physiology: A review. *Frontiers in Physiology*, 13, 2022.

[26] J. W. Gibbs. Principles of statistical mechanics. *Elementary Principles in Statistical Mechanics, New York: Charles Scribner's Sons*, 1902.

[27] M. N. Gibbs and D. J. MacKay. Variational gaussian process classifiers. *IEEE Transactions on Neural Networks*, 11(6):1458–1464, 2000.

[28] D. E. Goldman. Potential, impedance, and rectification in membranes. *The Journal of general physiology*, 27(1):37–60, 1943.

[29] S. Gora, D. Elad, and A. J. Jaffa. Objective analysis of vaginal ultrasound video clips for exploring uterine peristalsis post vaginal and cesarean section deliveries. *Reproductive Sciences*, 25(6):899–908, 2018.

[30] E. Hadar, T. Biron-Shental, O. Gavish, O. Raban, and Y. Yogev. A comparison between electrical uterine monitor, tocodynamometer and intra uterine pressure catheter for uterine activity in labor. *The Journal of Maternal-Fetal & Neonatal Medicine*, 28(12):1367–1374, 2015.

[31] C.-M. Hai and R. A. Murphy. Cross-bridge phosphorylation and regulation of latch state in smooth muscle. *American Journal of Physiology-Cell Physiology*, 254(1):C99–C106, 1988.

[32] S. M. Hawkins and M. M. Matzuk. The menstrual cycle: basic biology. *Annals of the New York Academy of Sciences*, 1135(1):10–18, 2008.

[33] A. L. Hodgkin and A. F. Huxley. A quantitative description of membrane current and its application to conduction and excitation in nerve. *The Journal of physiology*, 117(4):500–544, 1952.

[34] E. Hodnett. Patient control during labor effects of two types of fetal monitors. *Journal of Obstetric, Gynecologic, & Neonatal Nursing*, 11(2):94–99, 1982.

[35] G. A. Holzapfel and R. W. Ogden. Constitutive modelling of passive myocardium: a structurally based framework for material characterization. *Philosophical Transactions of the Royal Society A: Mathematical, Physical and Engineering Sciences*, 367(1902):3445–3475, 2009.

[36] G. Houzeaux, R. Aubry, and M. Vázquez. Extension of fractional step techniques for incompressible flows: The preconditioned orthomin (1) for the pressure schur complement. *Computers & Fluids*, 44(1):297–313, 2011.

[37] G. Houzeaux, M. Vázquez, R. Aubry, and J. M. Cela. A massively parallel fractional step solver for incompressible flows. *Journal of Computational Physics*, 228(17):6316–6332, 2009.

[38] J. D. Humphrey. Continuum biomechanics of soft biological tissues. *Proceedings of the Royal Society of London. Series A: Mathematical, Physical and Engineering Sciences*, 459(2029):3–46, 2003.

[39] P. J. Hunter, A. D. McCulloch, and H. Ter Keurs. Modelling the mechanical properties of cardiac muscle. *Progress in biophysics and molecular biology*, 69(2-3):289–331, 1998.

[40] G. Hutchings, O. Williams, D. Cretoiu, and S. M. Ciontea. Myometrial interstitial cells and the coordination of myometrial contractility. *Journal of cellular and molecular medicine*, 13(10):4268–4282, 2009.

[41] F. Hytten, G. Cheyne, et al. The size and composition of the human pregnant uterus. *Journal of Obstetrics and Gynaecology of the British Commonwealth*, 76:400–403, 1969.

[42] Y. Inoue, K. Okabe, and H. Soeda. Augmentation and suppression of action potentials by estradiol in the myometrium of pregnant rat. *Canadian journal of physiology and pharmacology*, 77(6):447–453, 1999.

[43] S. Jain, A. F. Saad, and S. S. Basraon. Comparing uterine electromyography & tocodynamometer to intrauterine pressure catheter for monitoring labor. *Journal of Woman's Reproductive Health*, 1(3):22–30, 2016.

[44] A. Kido, K. Togashi, M. Nishino, K. Miyake, T. Koyama, R. Fujimoto, K. Iwasaku, S. Fujii, and K. Hayakawa. Cine mr imaging of uterine peristalsis in patients with endometriosis. *European radiology*, 17:1813–1819, 2007.

[45] S. Kissler, E. Siebzehnruebl, J. Kohl, A. Mueller, N. Hamscho, R. Gaetje, A. Ahr, A. Rody, and M. Kaufmann. Uterine contractility and directed sperm transport assessed by hysterosalpingoscintigraphy (hssg) and intrauterine pressure (iup) measurement. *Acta obstetricia et gynecologica Scandinavica*, 83(4):369–374, 2004.

[46] N. Kuijsters, F. Sammali, C. Rabotti, Y. Huang, M. Mischi, and B. C. Schoot. Visual inspection of transvaginal ultrasound videos to characterize uterine peristalsis: an inter-observer agreement study. *Journal of Ultrasound*, 23:37–44, 2020.

[47] N. P. M. Kuijsters, W. G. Methorst, M. S. Q. Kortenhorst, C. Rabotti, M. Mischi, and B. C. Schoot. Uterine peristalsis and fertility: current knowledge and future perspectives: a review and meta-analysis. *Reproductive biomedicine online*, 35(1):50–71, 2017.

[48] G. Kunz and G. Leyendecker. Uterine peristaltic activity during the menstrual cycle: characterization, regulation, function and dysfunction. *Reproductive biomedicine online*, 4:5–9, 2002.

[49] P. S. La Rosa, H. Eswaran, H. Preissl, and A. Nehorai. Multiscale forward electromagnetic model of uterine contractions during pregnancy. *BMC medical physics*, 12(1):1–16, 2012.

[50] P. Lafortune, R. Arís, M. Vázquez, and G. Houzeaux. Coupled electromechanical model of the heart: parallel finite element formulation. *International journal for numerical methods in biomedical engineering*, 28(1):72–86, 2012.

[51] B. K. Lind. The frequency of extramembranous placement of intrauterine pressure catheters. *Primary Care Update for Ob/Gyns*, 5(4):185, 1998.

[52] S. Liu, Q. Zhang, C. Yin, S. Liu, Q. Chan, W. Chen, J. He, and B. Zhu. Optimized approach to cine mri of uterine peristalsis. *Journal of Magnetic Resonance Imaging*, 44(6):1397–1404, 2016.

[53] C. Maffeo, S. Bhattacharya, J. Yoo, D. Wells, and A. Aksimentiev. Modeling and simulation of ion channels. *Chemical reviews*, 112(12):6250–6284, 2012.

[54] P. Massó, A. Callejas, J. Melchor, F. S. Molina, and G. Rus. In vivo measurement of cervical elasticity on pregnant women by torsional wave technique: A preliminary study. *Sensors*, 19(15):3249, 2019.

[55] E. McCleskey, A. Fox, D. Feldman, and R. Tsien. Different types of calcium channels. *Journal of experimental biology*, 124(1):177–190, 1986.

[56] M. C. McCormick, J. S. Litt, V. C. Smith, and J. A. Zupancic. Prematurity: an overview and public health implications. *Annual review of public health*, 32:367–379, 2011.

[57] A. McEvoy and S. Sabir. Physiology, pregnancy contractions. 2018.

[58] M. Mihm, S. Gangooly, and S. Muttukrishna. The normal menstrual cycle in women. *Animal reproduction science*, 124(3-4):229–236, 2011.

[59] J. Mironneau. Effects of oxytocin on ionic currents underlying rhythmic activity and contraction in uterine smooth muscle. *Pflügers Archiv*, 363(2):113–118, 1976.

[60] A. Nakai, K. Togashi, T. Yamaoka, T. Fujiwara, H. Ueda, T. Koyama, H. Kobayashi, T. Kagimura, S. Fujii, and J. Konishi. Uterine peristalsis shown on cine mr imaging using ultrafast sequence. *Journal of Magnetic Resonance Imaging: An Official Journal of the International Society for Magnetic Resonance in Medicine*, 18(6):726–733, 2003.

[61] K. Nakao, Y. Inoue, K. Okabe, T. Kawarabayashi, and K. Kitamura. Oxytocin enhances action potentials in pregnant human myometrium—a study with microelectrodes. *American journal of obstetrics and gynecology*, 177(1):222–228, 1997.

[62] R. B. Newman. Uterine contraction assessment. *Obstetrics and Gynecology Clinics*, 32(3):341–367, 2005.

[63] S. Niederer, P. Hunter, and N. Smith. A quantitative analysis of cardiac myocyte relaxation: a simulation study. *Biophysical journal*, 90(5):1697–1722, 2006.

[64] Y. Otsubo, M. Nishida, Y. Arai, R. Ichikawa, A. Taneichi, and M. Sakanaka. Association of uterine wall thickness with pregnancy outcome following uterine-sparing surgery for diffuse uterine adenomyosis. *Australian and New Zealand Journal of Obstetrics and Gynaecology*, 56(1):88–91, 2016.

[65] G. Pfitzer. Invited review: regulation of myosin phosphorylation in smooth muscle. *Journal of applied physiology*, 91(1):497–503, 2001.

[66] C. O. Rees, A. de Boer, Y. Huang, B. Wessels, C. Blank, N. Kuijsters, A. Huppelschoten, B. Zizolfi, V. Foreste, A. D. S. Sardo, et al. Uterine contractile activity in healthy women throughout the menstrual cycle measured using a novel quantitative two-dimensional transvaginal ultrasound speckle tracking method. *Reproductive BioMedicine Online*, 46(1):115–122, 2023.

[67] S. Rihana, J. Santos, S. Mondie, and C. Marque. Dynamical analysis of uterine cell electrical activity model. In *2006 International Conference of the IEEE Engineering in Medicine and Biology Society*, pages 4179–4182. IEEE, 2006.

[68] J. M. Rogers and A. D. McCulloch. A collocation-galerkin finite element model of cardiac action potential propagation. *IEEE Transactions on Biomedical Engineering*, 41(8):743–757, 1994.

[69] R. Romero, S. K. Dey, and S. J. Fisher. Preterm labor: one syndrome, many causes. *Science*, 345(6198):760–765, 2014.

[70] A. Salamanca and E. Beltrán. Subendometrial contractility in menstrual phase visualized by transvaginal sonography in patients with endometriosis. *Fertility and sterility*, 1(64):193–195, 1995.

[71] K. M. Sanders. A case for interstitial cells of cajal as pacemakers and mediators of neurotransmission in the gastrointestinal tract. *Gastroenterology*, 111(2):492–515, 1996.

[72] A. Santiago, J. Aguado-Sierra, M. Zavala-Aké, R. Doste-Beltran, S. Gómez, R. Arís, J. C. Cajas, E. Casoni, and M. Vázquez. Fully coupled fluid-electro-mechanical model of the human heart for supercomputers. *International journal for numerical methods in biomedical engineering*, 34(12):e3140, 2018.

[73] F. Shitano, A. Kido, M. Kataoka, K. Fujimoto, K. Kiguchi, Y. Fushimi, and K. Togashi. Evaluation of uterine peristalsis using cine mri on the coronal plane in comparison with the sagittal plane. *Acta Radiologica*, 57(1):122–127, 2016.

[74] E. Tamilia, F. Taffoni, D. Formica, L. Ricci, E. Schena, F. Keller, and E. Guglielmelli. Technological solutions and main indices for the assessment of newborns' nutritive sucking: a review. *Sensors*, 14(1):634–658, 2014.

[75] K. M. Thijssen, J. G. Tissink, J. P. Dieleman, M. B. Van der Hout-van, M. E. Westerhuis, S. G. Oei, et al. Qualitative assessment of interpretability and observer agreement of three uterine monitoring techniques. *European Journal of Obstetrics & Gynecology and Reproductive Biology*, 255:142–146, 2020.

[76] W.-C. Tong, C. Y. Choi, S. Karche, A. V. Holden, H. Zhang, and M. J. Taggart. A computational model of the ionic currents, ca2+ dynamics and action potentials underlying contraction of isolated uterine smooth muscle. *PloS one*, 6(4):e18685, 2011.

[77] W.-C. Tong, R. M. Tribe, R. Smith, and M. J. Taggart. Computational modeling reveals key contributions of kcnq and herg currents to the malleability of uterine action potentials underpinning labor. *PloS one*, 9(12):e114034, 2014.

[78] M. Vázquez, R. Arís, J. Aguado-Sierra, G. Houzeaux, A. Santiago, M. López, P. Córdoba, M. Rivero, and J. Cajas. Alya red ccm: Hpc-based cardiac computational modelling. In *Selected topics of computational and experimental fluid mechanics*, pages 189–207. Springer, 2015.

[79] M. Vázquez, R. Arís, G. Houzeaux, R. Aubry, P. Villar, J. Garcia-Barnés, D. Gil, and F. Carreras. A massively parallel computational electrophysiology model of the heart. *International journal for numerical methods in biomedical engineering*, 27(12):1911–1929, 2011.

[80] M. Vázquez, G. Houzeaux, S. Koric, A. Artigues, J. Aguado-Sierra, R. Aris, D. Mira, H. Calmet, F. Cucchietti, H. Owen, et al. Alya: Towards exascale for engineering simulation codes. arxiv. org (2014).

[81] H. Wang and Y. Wang. Spatial-dependent regularization to solve the inverse problem in electromyometrial imaging. *Medical & biological engineering & computing*, 58:1651–1665, 2020.

[82] H. Wang, Z. Wen, W. Wu, Z. Sun, Z. Kisrieva-Ware, Y. Lin, S. Wang, H. Gao, H. Xu, P. Zhao, et al. Noninvasive electromyometrial imaging of human uterine maturation during term labor. *Nature Communications*, 14(1):1198, 2023.

[83] H. Wang, W. Wu, M. Talcott, R. C. McKinstry, P. K. Woodard, G. A. Macones, A. L. Schwartz, P. Cuculich, A. G. Cahill, and Y. Wang. Accuracy of electromyometrial imaging of uterine contractions in clinical environment. *Computers in biology and medicine*, 116:103543, 2020.

[84] S. Wang, K. Anderson, S. Pizzella, H. Xu, Z. Wen, Y. Lin, Y. Nan, J. Lau, Q. Wang, V. Ratts, et al. Noninvasive electrophysiological imaging identifies 4d uterine peristalsis patterns in subjects with normal menstrual cycles and patients with endometriosis. 2023.

[85] Y. Wang, X. Li, N. Wei, Y. Liu, X. Liu, R. Sun, C. Huang, B. Yao, and H. Wang. Automated measurement of endometrial peristalsis in cine transvaginal ultrasound images. *Frontiers in Physiology*, 13:983177, 2022.

[86] S. Weiss, T. Jaermann, P. Schmid, P. Staempfli, P. Boesiger, P. Niederer, R. Caduff, and M. Bajka. Three-dimensional fiber architecture of the nonpregnant human uterus determined ex vivo using magnetic resonance diffusion tensor imaging. *The Anatomical Record Part A: Discoveries in Molecular, Cellular, and Evolutionary Biology: An Official Publication of the American Association of Anatomists*, 288(1):84–90, 2006.

[87] D. Wilde and J. Marshall. Effects of tetraethylammonium and 4-aminopyridine on the plateau potential of circular myometrium from the pregnant rat. *Biology of reproduction*, 38(4):836–845, 1988.

[88] W. Wu, H. Wang, P. Zhao, M. Talcott, S. Lai, R. C. McKinstry, P. K. Woodard, G. A. Macones, A. L. Schwartz, A. G. Cahill, et al. Noninvasive high-resolution electromyometrial imaging of uterine contractions in a translational sheep model. *Science translational medicine*, 11(483):eaau1428, 2019.

[89] J. Yang, J. W. Clark Jr, R. M. Bryan, and C. Robertson. The myogenic response in isolated rat cerebrovascular arteries: smooth muscle cell model. *Medical engineering & physics*, 25(8):691–709, 2003.

[90] Z.-M. Yang, D.-B. Chen, S.-P. Le, and M. J. Harper. Differential hormonal regulation of leukemia inhibitory factor (lif) in rabbit and mouse uterus. *Molecular Reproduction and Development: Incorporating Gamete Research*, 43(4):470–476, 1996.

[91] M. Yochum, J. Laforêt, and C. Marque. An electro-mechanical multiscale model of uterine pregnancy contraction. *Computers in biology and medicine*, 77:182–194, 2016.

[92] M. Yochum, J. Laforêt, and C. Marque. Uterine smooth muscle cell force generation from electrical properties. In *BioMedWomen*, pages 41–44. CRC Press, 2016.

[93] M. Yochum, J. Laforêt, and C. Marque. Multi-scale and multi-physics model of the uterine smooth muscle with mechanotransduction. *Computers in Biology and Medicine*, 93:17–30, 2018.

[94] M. Yoshino, S. Wang, and C. Kao. Sodium and calcium inward currents in freshly dissociated smooth myocytes of rat uterus. *The Journal of general physiology*, 110(5):565–577, 1997.

[95] H. A. Zafrah and M. F. Alotaibi. The effect of extracellular atp on rat uterine contraction from different gestational stages and its possible mechanisms of action. *Journal of basic and clinical physiology and pharmacology*, 28(3):209–217, 2017.

[96] M. Zhang, P. S. La Rosa, H. Eswaran, and A. Nehorai. Estimating uterine source current during contractions using magnetomyography measurements. *PloS one*, 13(8):e0202184, 2018.

[97] M. Zhang, V. Tidwell, P. S. La Rosa, J. D. Wilson, H. Eswaran, and A. Nehorai. Modeling magnetomyograms of uterine contractions during pregnancy using a multiscale forward electromagnetic approach. *PloS one*, 11(3):e0152421, 2016.

[98] Y. Zhang, J. Qian, O. Zaltzhendler, M. Bshara, A. J. Jaffa, D. Grisaru, E. Duan, and D. Elad. Analysis of in vivo uterine peristalsis in the non-pregnant female mouse. *Interface Focus*, 9(4):20180082, 2019.